Innate–adaptive IFN cross-talk reprograms myeloid and T cells for antitumor immunity with a second-generation recombinant MVA

Shuaitong Liu[1,2#], Yueqi Wang[1,2,10#], Gregory Mazo[1#], Shanza Baseer Tariq[1,2], Juan Angulo-Lozano[2], Ning Yang[1], Tuo Zhang[5], Yi Wang[1,2], Daniel Hirschhorn[3,4,10], Liangliang Ji[8], Adrian Tan[5], Jiahu Wang[6], Wei Yan[7], John Choi[7], Jenny Zhaoying Xiang[5], Ming O. Li[8], Taha Merghoub[3,4,10], Jedd D. Wolchok[3,4,10], Charles M. Rice[2], and Liang Deng[1,2,9,11]*

[1]Dermatology Service, Department of Medicine, Memorial Sloan Kettering Cancer Center, New York, NY, USA.

[2]Laboratory of Virology and Infectious Disease, The Rockefeller University, New York, NY, USA.

[3]Swim Across America and Ludwig Collaborative Laboratory, Department of Pharmacology, Weill Cornell Medicine, New York, NY, USA

[4]Sandra and Edward Meyer Cancer Center, Weill Cornell Medicine, New York, NY, USA.

[5]Genomic Resources Core Facility, Weill Cornell Medical College, New York, NY, USA.

[6]Genvira Biosciences, Ottawa, ON K1V 1C1, Canada.

[7]IMVAQ Therapeutics, Sammamish, WA, 98021, USA.

[8]Immunology Program, Memorial Sloan Kettering Cancer Center, New York, NY, USA.

[9]Human Oncology and Pathogenesis Program; Memorial Sloan Kettering Cancer Center, New York, NY, USA.

[10]Parker Institute for Cancer Immunotherapy, San Francisco, CA, USA.

[11]Department of Dermatology, Weill Cornell Medical College, New York, NY, USA.

*corresponding author. Mailing address for Liang Deng: Dermatology Service, Department of Medicine, Memorial Sloan Kettering Cancer Center, New York, NY, USA. Email: dengl@mskcc.org. [#]These three authors contributed equally to this work.

Short running title: IFN Cross-Talk Reprograms Myeloid and T Cells in rMVA Therapy

SUMMARY

Resistance to immune checkpoint blockade (ICB) remains a major obstacle in cancer immunotherapy. We rationally engineered a second-generation recombinant Modified Vaccinia virus Ankara (MQ833) by deleting viral immune-evasion genes (*E3L*, *E5R*, *WR199*) and incorporating *Flt3L*, *OX40L*, and matrix-anchored *IL12*. Intratumoral MQ833 elicited robust tumor regressions across multiple models, including ICB-resistant and MHC-I–deficient tumors. Single-cell RNA sequencing revealed extensive remodeling of the tumor microenvironment, characterized by neutrophil and monocyte recruitment and activation, M2 macrophage depletion, M1 polarization, and effector T-cell differentiation and proliferation. Conditional *Ifnar1* knockout mice demonstrated that MQ833 efficacy requires type I interferon signaling in neutrophils, macrophages/monocytes, and T cells. Moreover, *Nos2* deficiency impaired therapeutic efficacy, confirming iNOS^{+} myeloid cells as key effectors. Together, these findings show that MQ833 activates innate–adaptive IFN cross-talk to reprogram myeloid and T cells, defining a rationally designed viral immunotherapy capable of overcoming ICB resistance.

Keywords: Modified Vaccinia Virus Ankara, viral immunotherapy, cancer immunotherapy, immune checkpoint blockade resistance, tumor microenvironment, type I interferon signaling, innate–adaptive cross-talk, myeloid cells, iNOS^{+} neutrophils, T-cell activation

GRAPHIC ABSTRACT

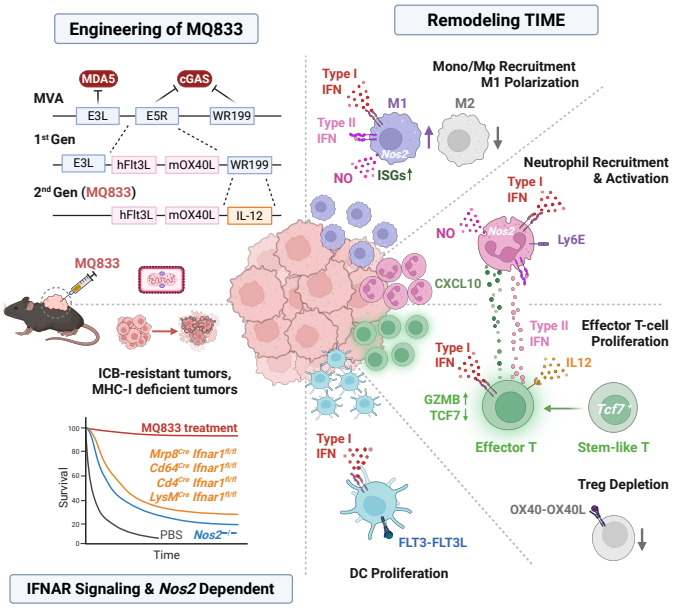

INTRODUCTION

47 The tumor immune microenvironment (TIME) comprises diverse populations of myeloid and
48 lymphoid cells whose antitumor functions are often subverted by the immunosuppressive milieu
49 of growing tumors.[1-3] A central challenge of cancer immunotherapy is to reprogram myeloid
50 cells and reinvigorate T cells to sustain antitumor immunity.[4-7] Among various approaches to
51 overcome immune resistance, immunogenic viruses have emerged as potent tools to remodel the
52 TIME and activate both innate and adaptive immunity.[8-11] However, accumulating evidence
53 suggests that viral replication and oncolysis are not essential for therapeutic efficacy; instead,
54 activation of innate sensing and local inflammation are the dominant drivers of viral-induced
55 antitumor immunity.[12-16]

56 Modified Vaccinia virus Ankara (MVA) is a large, non-replicative cytoplasmic DNA virus
57 derived from the replication-competent vaccinia Ankara strain after more than 500 passages in
58 chicken embryonic fibroblasts, resulting in extensive deletions in host range and immune evasion
59 genes.[17,18] MVA was recently approved as a vaccine against smallpox and mpox [19], and has been
60 intensively studied as a vector for vaccines and cancer immunotherapies.[20,21] Its favorable safety
61 profile, large genomic capacity for transgene insertion, and ability to infect both tumor and
62 immune cells make it an attractive backbone for rational vector design.

63 We previously showed that MVA infection of dendritic cells activates the cytosolic DNA-
64 sensing pathway via cyclic GMP–AMP synthase (cGAS) and induces moderate type I interferon
65 (IFN) production.[22] Intratumoral (IT) injection of heat-inactivated MVA generates potent $CD8^+$
66 T-cell–dependent antitumor immunity through cGAS–STING signaling.[14] Furthermore, we
67 demonstrated that heat-inactivated oncolytic vaccinia virus elicited stronger antitumor effects
68 than its replicating counterpart,[15] supporting the concept that immunogenic viral activation,
69 rather than direct oncolysis, is sufficient to drive tumor regression. These findings established the
70 basis for developing non-replicative, immunostimulatory MVA vectors for cancer
71 immunotherapy.

72 Building on this foundation, we engineered a first-generation recombinant MVA (*rMVA*,
73 MQ710) by deleting *E5R*, an inhibitor of cGAS, and inserting human *Flt3L* and murine *OX40L*

to enhance dendritic-cell recruitment and regulatory T-cell depletion via OX40–OX40L and IFNAR signaling.[23] Intratumoral delivery of MQ710 exhibited potent antitumor activity in murine models and is currently being evaluated in a Phase I clinical trial for advanced solid tumors (NCT05859074) with promising early results.

To further amplify immunogenicity and define the mechanistic basis of viral-induced antitumor immunity, we designed a second-generation rMVA, MQ833. MQ833 was engineered through deletion of three viral immune-suppressive genes (*E3L*, *E5R*, and *WR199*) and insertion of *Flt3L*, *OX40L*, and an extracellular matrix–anchored *IL12* transgene to enhance local cytokine activity while minimizing systemic toxicity. *E3L* encodes a double-stranded RNA–binding protein that suppresses MDA5-mediated sensing,[24,25] whereas *WR199* inhibits cGAS activation;[26] their removal was intended to potentiate both MDA5- and STING-dependent type I IFN signaling.

Here, we evaluated the therapeutic efficacy and mechanistic underpinnings of MQ833 across multiple murine tumor models, including melanoma, colon carcinoma, and bladder cancer. We used single-cell RNA sequencing to dissect how MQ833 reprograms the TIME, with particular focus on nucleic acid–sensing pathways and type I IFN–driven myeloid and T-cell activation. These studies define a mechanistically optimized recombinant platform that integrates rational viral engineering with localized cytokine delivery to orchestrate coordinated innate and adaptive immune activation against solid tumors

92 **RESULTS**

93 **Rational engineering of MQ833 amplifies innate sensing and T cell activation**

94 Our previous work identified the vaccinia E5R gene as a potent inhibitor of the DNA sensor
95 cGAS. Deletion of E5R from MVA (MVAΔE5R) induced high levels of IFN-β in bone marrow-
96 derived dendritic cells (BMDCs) in a cGAS-dependent manner.[26] Based on this backbone, we
97 generated our first-generation recombinant virus, rMVA (MQ710; MVAΔE5R-hFlt3L-
98 mOX40L), which expresses membrane-bound human Flt3L and murine OX40L. Intratumoral
99 (IT) delivery of MQ710 elicited strong antitumor immunity across multiple tumor models,
100 dependent on $CD8^+$ T cells, cGAS/STING, and IFNAR signaling, and also depleted intratumoral
101 $OX40^{hi}$ Tregs through OX40L–OX40 and IFNAR-mediated mechanisms.[23]

102 To further overcome viral immune evasion, we deleted additional inhibitory genes—E3L, which
103 blocks cytosolic dsRNA sensing,[25] and WR199 (MVA186), recently identified as a cGAS
104 inhibitor.[27] Deleting *E3L* together with *E5R* markedly increased *Ifnb* induction across multiple
105 murine tumor cell lines, whereas single deletions yielded only modest effects (Figure S1A).
106 Mechanistically, MVAΔE3LΔE5R triggered strong IRF3 phosphorylation and IFN-β production
107 in WT but not in *Mda5*$^{-/-}$ or *Mda5*$^{-/-}$*Sting*$^{-/-}$ tumor cells (Figure S1B and Figure S1C),
108 confirming predominant dependence on MDA5 pathways.

109 In vivo, deletion of *E3L* enhanced tumor-specific T-cell priming. In a bilateral B16-F10 model,
110 IT rMVAΔE3L induced a higher frequency of IFN-γ–secreting splenic $CD8^+$ T cells compared
111 with rMVA (Figure S2A-C). Further deletion of *WR199* produced MQ832
112 (MVAΔE5RΔE3LΔWR199-hFlt3L-mOX40L), which modestly increased $CD8^+$ T-cell activation
113 and further decreased $OX40^{hi}$ Tregs compared with rMVAΔE3L (Figure S2D and Figure S2E).

114 To potentiate T/NK-cell activation while minimizing systemic cytokine toxicity, we inserted a
115 bicistronic IL-12 cassette (Il12a–P2A–Il12b) under a modified H5 early/later promoter into the
116 *WR199* locus and tagged the IL-12p35 subunit with an extracellular matrix-binding sequence to
117 localize cytokine activity to the tumor microenvironment, generating MQ833
118 (MVAΔE5RΔE3LΔWR199-hFlt3L-mOX40L-mIL12) (Figure 1A and Figure 1B). [28,29]

119 MQ833 infection induced robust transgene expression of hFlt3L and mOX40L, along with high
120 levels of IL-12p40 secretion (Figure 1C and Figure 1D). MQ833 markedly upregulated *Ifnb*
121 transcripts and IFN-β secretion in B16-F10 cells compared with MVA or MVAΔE5R (Figure 1E
122 and Figure 1F). Western blot analysis showed enhanced STING and IRF3 phosphorylation
123 beginning at 4 hours post infection (hpi), confirming strong activation of the cGAS/STING
124 pathway (Figure 1G). Consistently, MQ833 induced high levels of STING-dependent IFN-β
125 production and p-IRF3 in BMDCs from WT but not *Sting*$^{Gt/Gt}$ mice (Figure 1H and Figure 1I).

126 Functionally, MQ833 enhanced antigen cross-presentation and T-cell activation. Splenic CD11c^{+}
127 DCs from WT or *cGAS*$^{-/-}$ mice infected with MQ833 and pulsed with OVA protein stimulated
128 stronger OT-I T-cell IFN-γ responses than MVAΔE5R, with partial dependence on cGAS
129 (Figure 1J and Figure 1K). Similar results were obtained with CD103^{+} DCs isolated from Flt3L-
130 expanded BMDCs (Figure 1L). Conditioned medium from infected BMDCs induced minimal
131 IFN-γ secretion compared with direct DC–T-cell coculture, indicating a contact-dependent
132 mechanism (Figure 1M).

133 Finally, we evaluated a humanized version of MQ833 (hMQ833; MVAΔE5RΔE3LΔWR199-
134 hFlt3L-hOX40L-hIL12) in human monocyte-derived dendritic cells (moDCs). Infection with
135 hMQ833 led to strong hFlt3L/hOX40L surface expression and secretion of IL-12p70,
136 accompanied by increased IFNB and CXCL10 transcription (Figure S3A-C). In co-culture
137 assays, hMQ833-primed moDCs stimulated both allogeneic and autologous CD4^{+} and CD8^{+} T
138 cells to secrete IFN-γ, with the most pronounced activation observed in allogeneic CD4^{+} T cells
139 (Figure S3D and S3E).

140 Together, these results demonstrate that sequential deletion of viral immune evasion genes (*E5R*,
141 *E3L*, *WR199*) synergistically enhances type I IFN induction through MDA5/STING signaling,
142 while incorporation of extracellular matrix-bound IL-12 amplifies antigen cross-presentation and
143 T-cell activation. MQ833 thus represents a second-generation recombinant MVA platform that
144 coordinates innate–adaptive IFN cross-talk to overcome tumor immunosuppression.

145 **MQ833 induces superior antitumor activity through type I IFN and nucleic acid–sensing**
146 **pathways**

147 Having established that MQ833 infection of tumor and immune cells activates the cGAS/STING
148 pathway and drives type I IFN production (Figure 1; Figures S1–S3), we next examined whether
149 this enhanced innate sensing translates into superior antitumor efficacy in vivo. MQ833 differs
150 from its predecessor MQ832 by incorporating an extracellular-matrix–anchored IL-12 cassette in
151 addition to deletions of three viral immune-evasion genes (*E5R*, *E3L*, and *WR199*). This design
152 was intended to further amplify local T- and NK-cell activation while minimizing systemic
153 cytokine toxicity.

154 In the B16-F10 melanoma model, intratumoral (IT) administration of MQ833 resulted in
155 complete tumor regression in all treated mice, whereas MQ832 produced partial responses with
156 40 % long-term survival (Figure 2A–2D). In the MC38 colon carcinoma model, MQ833 also
157 outperformed MQ832, curing 100% of mice compared with 30% for MQ832 (Figures S4A–
158 S4B).

159 To assess systemic or abscopal effects, we next used a bilateral MC38 model with higher tumor
160 burden, IT MQ833 delayed the growth of both injected and contralateral tumors and significantly
161 prolonged survival relative to MQ832 (Figures S4C–S4E). Similar results were obtained in a
162 bilateral B16-F10 model. We observed that IT MQ833 eradicated most injected tumors,
163 markedly suppressed growth of contralateral non-injected lesions, and achieved cures in 40% of
164 mice, whereas MQ832 produced no long-term survivors (Figures S5A–S5C). Combination
165 therapy of IT MQ833 with systemic immune-checkpoint blockade (ICB) using anti-PD-1, anti-
166 PD-L1, or anti-CTLA-4 antibodies further improved outcomes, curing 60 % of mice (Figures
167 S5A–S5C). These findings demonstrate that MQ833 elicits potent local and systemic antitumor
168 immunity that can be synergistically enhanced by ICB.

169 Flow-cytometric analyses of injected and non-injected tumors revealed that both MQ833 and
170 MQ832 increased Granzyme B^+ and $KLRG1^+$ effector $CD8^+$ T cells while reducing $Foxp3^+$
171 regulatory T cells, but MQ833 induced a more pronounced and sustained Treg depletion across
172 both tumor sites (Figure 2E–2F; Figures S5E–S5F).

173 Given its design to activate both dsRNA- and DNA-sensing pathways, we next evaluated
174 MQ833 activity in mice deficient for *Mda5*, *Sting*, or both. IT MQ833 cured 81% of WT mice

175 but only 45%, 46%, and 40% cure in *Sting*$^{Gt/Gt}$, *Mda5*$^{-/-}$, and *Sting*$^{Gt/Gt}$*Mda5*$^{-/-}$ mice, respectively
176 (Figure 2G–2H), indicating that both MDA5- and STING-mediated nucleic-acid sensing
177 contribute to its therapeutic efficacy. Furthermore, *Stat2*$^{-/-}$ mice responded poorly, with only
178 11% cures, confirming that type I IFN signaling through STAT2 is essential for MQ833-induced
179 antitumor immunity (Figure 2G–2H).

180 Together, these results demonstrate that MQ833 engages dual nucleic-acid–sensing and type I
181 IFN pathways to orchestrate coordinated innate and adaptive immune activation, resulting in
182 complete and durable tumor regression in multiple preclinical models.

183 **MQ833 remodels myeloid and T-cell compartments in the tumor microenvironment**

184 We next used single-cell RNA sequencing (scRNA-seq) to define how MQ833 alters the tumor
185 immune microenvironment (TIME) and to assess the contributions of nucleic acid–sensing and
186 type I IFN pathways. CD45^{+} immune cells were sorted from B16-F10 tumors in WT mice,
187 *Sting*$^{Gt/Gt}$*Mda5*$^{-/-}$ (DKO), and Stat2$^{-/-}$ mice two days after IT MQ833, followed by scRNA-seq
188 analysis (Figure 3A). Unsupervised clustering identified 19 immune cell clusters, including
189 T/NK cells, monocytes/macrophages, neutrophils, dendritic cells, and B cells, along with minor
190 undefined and melanoma cell populations (Figure 3B and 3C). Cluster annotations were
191 validated by expression of canonical lineage markers (Figure 3C; Figure S6A).

192 In WT mice, MQ833 induced rapid recruitment of inflammatory monocytes and neutrophils,
193 which expanded from 1% to 29% and 0.3% to 12% of CD45^{+} cells, respectively (Figure 3D and
194 3E). This was accompanied by depletion of M2-like macrophages and increased M1-like
195 macrophages, as well as reduced intratumoral cDC1 frequencies, consistent with migration to
196 draining lymph nodes (Figure 3D and 3E). In DKO mice, neutrophil and monocyte recruitment
197 and M2 depletion were attenuated, and cDC1 activation was impaired (Figure 3D and 3E). In
198 *Stat2*$^{-/-}$ mice, MQ833 triggered expansion of M1-like macrophage and neutrophil clusters that
199 were transcriptionally distinct from their WT counterparts and lacked canonical IFN-stimulated
200 gene (ISG) expression (Figure 3D–E). Single-cell viral transcript mapping revealed that
201 neutrophils were the most heavily infected immune population (Figure S6B–S6C). Gene set
202 enrichment analysis revealed robust induction of IFN-α, IFN-γ, and TNF signaling programs in

203 MQ833-treated WT tumors, whereas oxidative phosphorylation and Myc targets were
204 suppressed (Figure 3F and 3G). Heatmaps of IFN-responsive genes showed broad upregulation
205 of ISGs, cytokines, and chemokines in WT mice, reduced responses in DKO mice, and complete
206 loss in Stat2$^{-/-}$ mice (Figure 3H).

207 Subclustering of CD3^{+} cells identified eight T-cell states: *Tcf7*$^{+}$ stem-like CD4, *Tcf7*$^{+}$*CD62L*$^{+}$
208 progenitor T cell, ISG^{+} CD8, early effector CD8, *Tox*^{int} effector CD8, proliferating effector T
209 cells, Th1 CD4, and Tregs (Figure 3I and 3J). In WT mice, MQ833 decreased *Tcf7*$^{+}$ stem-like
210 subsets and expanded early effector, effector, and proliferating CD8^{+} T cells (Figure 3K and 3L).
211 In DKO mice, differentiation into effector CD8^{+} subsets was attenuated, although proliferating
212 CD8^{+} T cells still expanded. In mock-treated *Stat2*$^{-/-}$ mice, *Tcf7*$^{+}$ stem-like populations
213 predominated, while effector subsets were absent. IT MQ833 in *Stat2*$^{-/-}$ mice reduced stem-like
214 populations and expanded proliferating CD8^{+} T cells, but failed to generate functional effectors,
215 indicating that IL-12 alone cannot compensate for the absence of type I IFN signaling (Figure 3K
216 and 3L). Pseudotime analysis revealed a continuous trajectory from stem-like to effector CD4^{+}
217 and CD8^{+} T cells in WT tumors (Figure 3M).

218 Together, these results demonstrate that MQ833 reprograms the myeloid compartment by
219 recruiting inflammatory monocytes and neutrophils, depleting M2-like macrophages, and
220 promoting M1 polarization. Concurrently, MQ833 drives T-cell differentiation toward effector
221 states in a manner dependent on MDA5/STING-mediated nucleic acid sensing and STAT2-
222 dependent type I IFN signaling.

223

224 **Type I IFN–STAT2 signaling governs the transcriptional polarization, but not recruitment,**
225 **of MQ833-induced tumor-infiltrating neutrophils**

226

227 We next performed sub-clustering of tumor-infiltrating neutrophils to define their heterogeneity
228 and to assess how type I IFN signaling shapes their activation states. Neutrophils were scarce at
229 baseline but were robustly recruited after MQ833 treatment. UMAP analysis identified eight
230 transcriptionally distinct neutrophil clusters (Figure 4A–4C). Clusters 1, 3, and 5 were enriched

231 in WT mice following treatment and were characterized by high expression of interferon-
232 stimulated genes (ISGs; *Ly6e, Isg15*) or *Nos2* (Figure 4D). The *ISG*^{high} *Ly6e*^{high} neutrophils
233 represent antitumoral, pro-inflammatory subsets, consistent with prior findings that *Ly6e*^{high}
234 neutrophils predict responsiveness to immunotherapy [30]. Elevated *Nos2* expression further
235 indicates tumoricidal potential through nitric-oxide-mediated cytotoxicity [31].

236 Although *Sting*$^{Gt/Gt}$*Mda5*$^{-/-}$ mice showed detectable neutrophil infiltration after MQ833 treatment,
237 the number and activation profiles of these cells were markedly reduced compared with WT
238 tumors. In WT mice, robust neutrophil recruitment was accompanied by strong induction of
239 *ISG*^{high} *Ly6e*^{high} and *Nos2*^{high} subsets, whereas in DKO mice, these populations were diminished
240 and displayed attenuated expression of interferon-stimulated genes (Figure 4E). In addition,
241 genes involved in the NF-kB pathway were also reduced in tumor-infiltrating CD45^{+} immune
242 cells from DKO mice compared with WT mice (Figure 7SC). Thus, MDA5 and STING jointly
243 promote both the recruitment and functional polarization of MQ833-induced tumor-infiltrating
244 neutrophils.

245 In contrast, *Stat2*$^{-/-}$ mice displayed transcriptionally divergent neutrophil clusters with markedly
246 diminished expression of IFN-α–response genes (Figure 4E). Differential expression analysis
247 (Figure 4F) revealed broad downregulation of canonical ISGs (*Ifit3, Isg15, Ly6c2, Ly6e, Stat2*),
248 chemokines mediating T-cell recruitment (*Cxcl10*), and immune-modulatory genes (*Il1rn, Fcgr1,*
249 *H2-Q7*). Pathway enrichment analysis (Figure 4G) demonstrated that MQ833-treated WT
250 neutrophils showed activation of IFN-α/γ, inflammatory, and TNF–NF-κB signaling programs,
251 whereas these pathways were blunted in *Stat2*$^{-/-}$ mice. Conversely, MYC-target and oxidative
252 phosphorylation programs were suppressed in WT but remained relatively enriched in *Stat2*$^{-/-}$
253 neutrophils.

254 Collectively, these results demonstrate that MQ833 reprograms tumor-infiltrating neutrophils
255 toward antitumoral and cytotoxic phenotypes, and that type I IFN–STAT2 signaling is
256 indispensable for sustaining their pro-inflammatory transcriptional state and effector function.

257 **Intratumoral MQ833 remodels the tumor immune landscape locally and systemically in a**
258 **bilateral melanoma model**

259 To delineate the local and systemic immune effects of MQ833 treatment, we employed a
260 bilateral B16-F10 melanoma model, in which the larger tumor received two intratumoral (IT)
261 injections of MQ833 while the contralateral lesion remained untreated. Two days after the
262 second injection, CD45$^+$ cells were isolated from injected, non-injected, and PBS-treated control
263 tumors and analyzed by single-cell RNA sequencing (Figure 5A). Unsupervised clustering
264 identified 14 major immune populations, including T and NK cells, multiple macrophage and
265 monocyte subsets, dendritic cells, neutrophils, and B cells (Figure 5B–C).

266 IT MQ833 markedly reshaped the myeloid compartment (Figure 5D–E). Neutrophils, nearly
267 absent in control tumors, became the dominant infiltrate in injected tumors but remained sparse
268 in distant lesions, indicating localized recruitment. Inflammatory monocytes and M1-like
269 macrophages expanded in both injected and non-injected tumors, while ISG$^+$ macrophages were
270 strongly enriched, particularly in the distant, non-injected tumors. In contrast, M2-like
271 macrophages were depleted across both sites. These data indicate that MQ833 promotes an IFN-
272 and inflammation-driven remodeling of the myeloid landscape, transforming suppressive
273 myeloid populations into antitumor proinflammatory states.

274 Sub-clustering of CD3$^+$ cells revealed nine transcriptionally distinct T-cell subsets (Figure 5F–
275 G), including *Tcf7*$^+$ stem-like T cells, ISG$^+$CD8$^+$, resident memory CD8$^+$, effector CD8$^+$,
276 *Tox*^{int}*Ifng*^{int} CD8, proliferating effector CD8, Th1 CD4$^+$ T cells, Tregs, and a small CD3$^+$
277 macrophage-like population. Following MQ833 treatment, effector, proliferating, and exhausted
278 CD8$^+$ T cells expanded markedly, particularly in the injected tumors, while ISG$^+$CD8$^+$, and stem-
279 like subsets contracted. Effector CD8$^+$ T cells also increased in the non-injected tumors,
280 consistent with the abscopal effects observed at distant sites. In contrast, Th1 CD4$^+$ T cells and
281 Tregs were reduced, whereas CD3$^+$ macrophage-like cells expressing *Lyz2*, *CD74*, *Ifitm3*,
282 *Fcer1g*, Ms4a6c, *H2-Ab1*, *H2-Aa*, *Cxcl2*, increased at both tumor sites.

283 Collectively, these data show that IT MQ833 induces a dual-layered immune response. Locally,
284 viral treatment triggers massive neutrophil recruitment, M1/ISG$^+$ macrophage polarization, and
285 proliferation of effector and exhausted CD8$^+$ T cells, establishing a proinflammatory, cytotoxic
286 milieu within injected tumors. Systemically, MQ833 promotes the expansion of ISG$^+$ and M1

287 macrophages, accumulation of effector CD8$^+$ T cells in distant, non-injected tumors—hallmarks
288 of an abscopal, IFN-driven reprogramming of the tumor immune microenvironment.

289 IFNAR signaling in both T cells and myeloid cells is required for the antitumor effects of 290 MQ833

291 To define the cellular mediators of MQ833-induced tumor regression, we performed antibody-
292 mediated depletion studies in the unilateral B16-F10 melanoma model (Figure 6A). Once tumors
293 were established, mice received intratumoral MQ833 twice weekly together with systemic
294 depletion of CD8$^+$ or CD4$^+$ T cells, NK1.1$^+$ cells, Ly6G$^+$ neutrophils, or CSF1-dependent
295 macrophages. Flow-cytometric analysis of peripheral blood confirmed efficient and selective
296 depletion for each target population (Figure S8A–C).

297 IT MQ833 alone achieved durable tumor clearance in more than half of treated animals, whereas
298 CD8$^+$ T-cell depletion completely abolished therapeutic benefit, confirming their indispensable
299 role in viral immunotherapy (Figure 6B–C). Strikingly, depletion of neutrophils or macrophages
300 also markedly reduced tumor control and survival, demonstrating that myeloid cells are essential
301 contributors to MQ833-driven antitumor efficacy. In contrast, depletion of CD4$^+$ T cells or NK
302 cells had minimal impact on early tumor regression (Figure 6B–C). Together, these data
303 establish that MQ833 engages a cooperative network of cytotoxic CD8$^+$ T cells, neutrophils, and
304 macrophages to mediate its potent therapeutic effects.

305 Because type I interferons orchestrate antiviral and antitumor inflammation, we next asked
306 whether IFNAR signaling in distinct immune compartments mediates MQ833-driven tumor
307 control. MB49-luc bladder tumors were implanted into conditional *Ifnar1*$^{fl/fl}$ mice lacking IFNAR
308 selectively in *Mrp8*$^+$ neutrophils, *Cd64*$^+$ macrophages, *LysM*$^+$ myeloid cells, or *Cd4*$^+$ T cells
309 (Figure 6D). IT MQ833 achieved 79% survival in *Ifnar1*$^{fl/fl}$ controls but only 50% in
310 *Mrp8*^{Cre}*Ifnar1*$^{fl/fl}$ mice, indicating that neutrophil-intrinsic IFNAR signaling contributes
311 substantially to antitumor efficacy (Figure 6E–F). Notably, all *Ifnar1*$^{fl/fl}$ mice that achieved tumor
312 clearance following MQ833 treatment resisted subsequent tumor rechallenge, whereas 60% of
313 *Mrp8*^{Cre}*Ifnar1*$^{fl/fl}$ mice failed to reject (Figure 6G), indicating that intact IFNAR signaling in
314 neutrophils is required not only for primary tumor control but also for the establishment of

315 durable antitumor memory. Loss of *Ifnar1* in *Cd64*$^+$ or *LysM*$^+$ myeloid cells similarly
316 compromised tumor rejection, underscoring the importance of myeloid-intrinsic type I IFN
317 signaling (Figure 6H-I). Deletion of *Ifnar1* in *Cd4*$^+$ T cells, which eliminates IFNAR1
318 expression in both CD4$^+$ and CD8$^+$ T-cell compartments, also partially reduced efficacy (Figure
319 6H–I), indicating that type I IFN signaling within T cells is critical for sustaining cytotoxic
320 effector differentiation and long-term antitumor immunity.

321 Collectively, these findings demonstrate that MQ833-induced tumor regression requires
322 coordinated IFNAR signaling across myeloid and T cells, which together orchestrate the
323 inflammatory and effector programs necessary for durable tumor eradication.

324 Nos2-dependent myeloid activation contributes to MQ833-induced antitumor 325 immunity

326 To determine whether MQ833 engages nitric oxide–mediated effector mechanisms, we analyzed
327 tumor-infiltrating immune cells two days after intratumoral injection. Flow cytometry revealed a
328 marked increase in iNOS$^+$ (Nos2$^+$) neutrophils and M1-like macrophages, accompanied by a
329 decrease in CD206$^+$ M2-like macrophages (Figure 7A–C), indicating that MQ833 polarizes the
330 myeloid compartment toward a proinflammatory phenotype.

331 We next evaluated whether Nos2 expression is required for the therapeutic activity of MQ833. In
332 WT mice bearing B16-F10 tumors, IT MQ833 resulted in 90% survival rate in WT mice and
333 only 40% survival rate in *Nos2*$^{-/-}$ mice (Figure 7D), establishing a key role for nitric oxide in
334 mediating tumor clearance.

335 Single-cell RNA-seq profiling of CD45$^+$ tumor-infiltrating cells showed that both MQ833 and
336 rMVAΔE3L expanded inflammatory monocytes and neutrophils while reducing M2
337 macrophages, but MQ833 uniquely upregulated *Nos2*, *Fas*, *Tnf*, *Cxcl1*, and *Cxcl10* in myeloid
338 clusters (Figure 7E–F; Figure S9A–C). Subclustering of CD3$^+$ cells further revealed that MQ833
339 promoted effector and effector-memory CD8$^+$ T cells (C5, C7) while depleting Tcf7$^+$ stem-like
340 subsets (Figure S9D–G). These coordinated changes reflect IL-12–driven CD8$^+$ T-cell
341 proliferation, activation, and IFN-γ production, which in turn induce *Nos2*$^+$ myeloid cells.

342 CXCL10 produced by these activated myeloid cells further enhances recruitment of effector T
343 cells into inflamed tumors.

344 Furthermore, MQ833 retained partial activity in *Rag1*$^{-/-}$ mice lacking T and B cells, prolonging
345 survival despite the absence of adaptive immunity (Figure 7G–I). Tumors from these mice
346 showed strong infiltration of iNOS^{+} neutrophils (Figure 7J–K), confirming that MQ833 can
347 mobilize innate cytotoxic programs independently of lymphocytes.

348 Finally, MQ833 was highly effective against *B2m*$^{-/-}$ B16-F10 tumors that lack MHC I and are
349 resistant to T-cell killing. IT MQ833 eradicated 70% of *B2m*$^{-/-}$ tumors, whereas control virus
350 MQ832 produced no cures (Figure 7L–M). All cured mice rejected rechallenge with WT B16-
351 F10 cells (Figure 7N), demonstrating durable systemic immunity.

352 Together, these results define a dual mechanism by which MQ833 orchestrates IL-12–induced,
353 IFN-γ–dependent activation of Nos2^{+} myeloid cells, which in turn synergize with adaptive T-cell
354 immunity to eliminate tumors, including that refractory to checkpoint blockade.
355

356 **DISCUSSION**

357 Viral-based cancer immunotherapy can remodel the tumor immune microenvironment (TIME) to
358 overcome both primary and acquired resistance to immune checkpoint blockade (ICB). Infection
359 of tumor and immune cells by recombinant viruses activates innate immune sensing, induces
360 immunogenic cell death, and promotes antigen-specific T-cell priming. Here, we describe the
361 rational engineering of a recombinant Modified Vaccinia virus Ankara (rMVA), MQ833,
362 through sequential deletion of three immune-evasion genes (*E3L*, *E5R*, and *WR199*) and
363 insertion of three immunostimulatory transgenes (*Flt3L*, *OX40L*, and *IL-12*), thereby amplifying
364 MDA5–STING–STAT2–dependent innate sensing and coordinating myeloid and T-cell
365 activation to elicit potent antitumor immunity.

366 Antibody-depletion studies established that CD8^{+} T cells, neutrophils, and macrophages are
367 indispensable for MQ833-mediated tumor regression. Using genetically engineered mice
368 deficient in nucleic-acid sensing or type I IFN signaling, we showed that MQ833 requires
369 MDA5/STING-driven cytosolic sensing and STAT2-dependent type I IFN signaling for durable

370 tumor control. Single-cell RNA sequencing (scRNA-seq) revealed that intratumoral MQ833
371 reprograms the TIME, driving inflammatory myeloid polarization and effector T-cell
372 differentiation. These results define MQ833 as a mechanistically engineered viral platform that
373 rewires innate–adaptive immunity to overcome immune evasion.

374 MQ833 infection triggers robust type I IFN and pro-inflammatory cytokine production through
375 MDA5/STING activation. Localized expression of extracellular-matrix-anchored IL-12 promotes
376 differentiation of $TCF7^{+}$ stem-like T cells into effector populations, augments IFN-γ production,
377 and polarizes macrophages toward an M1 phenotype. Concurrently, MQ833 recruits neutrophils,
378 where IFNAR/IFNGR signaling induces Nos2 expression and nitric oxide–mediated
379 cytotoxicity, transforming an immunosuppressed milieu into an IFN-driven cytotoxic network.

380 MQ833 builds upon the first-generation rMVA (MVAΔE5R-hFlt3L-mOX40L) by deleting E3L,
381 a dsRNA-binding protein that blocks MDA5 sensing, and WR199, a cGAS inhibitor. Combined
382 deletion of E5R and E3L synergistically enhanced type I IFN induction, while addition of IL-12
383 yielded maximal immune activation. This demonstrates that iterative, mechanism-based vector
384 design can amplify innate recognition without compromising viral stability.

385 Localized IL-12 expression increased effector $CD8^{+}$ T cells, reduced intratumoral Tregs, and
386 enhanced IFN-γ production in melanoma and colon-carcinoma models. scRNA-seq showed
387 expansion of effector $CD8^{+}$ T cells and upregulation of *Nos2*, *Fas*, *Tnf*, and *Cxcl10* in myeloid
388 clusters, indicating enhanced cytotoxic and chemotactic capacity. Efficacy was reduced in
389 *Nos2*$^{-/-}$ mice, establishing nitric oxide as a key effector linking innate and adaptive immunity and
390 underscoring that IL-12 and type I IFN signaling act in concert to sustain effector programs.

391 In addition to T-cell–mediated effects, MQ833 displayed $CD8^{+}$ T-cell–independent activity
392 through neutrophils and macrophages. Depletion of $Ly6G^{+}$ neutrophils or CSF1-dependent
393 macrophages abrogated efficacy, while MQ833 delayed tumor growth in *Rag1*$^{-/-}$ mice and
394 eradicated MHC I–deficient tumors, indicating that MQ833 mobilizes both innate and adaptive
395 effector programs—distinguishing it from prior oncolytic viruses dependent on T-cell killing.

396 Neutrophils displayed a prominent IFN-stimulated-gene (ISG) signature after viral treatment.
397 scRNA-seq identified *Ly6E*^{high} *ISG*^{high} and *Nos2*^{high} subsets consistent with antitumoral neutrophil

398 states. These subsets were diminished in *Mda5*$^{-/-}$ *Sting*$^{Gt/Gt}$ mice and absent in *Stat2*$^{-/-}$ mice,
399 demonstrating that type I IFN–STAT2 signaling governs neutrophil polarization. MQ833-
400 infected neutrophils upregulated Cxcl10, linking them to IFN-driven T-cell recruitment and
401 defining a neutrophil–T-cell cross-talk axis critical for viral immunotherapy.

402 Recent studies revealed that interferon-stimulated neutrophil states predict immunotherapy
403 outcomes. IFN-licensed neutrophils cooperate with T cells to eliminate antigen-escape variants,[31]
404 while conserved *ISG*$^{+}$*Nos2*$^{+}$ or *Ly6E*$^{+}$ subsets driven by tumor-intrinsic STING correlate with
405 tumor control.[30,32] The MQ833-induced Ly6E^{+}ISG^{+} neutrophils likely represent this IFN-
406 conditioned effector subset, bridging innate and adaptive immunity through coordinated IFNAR–
407 STAT2 and IL-12–IFN-γ–NOS2 signaling. These findings position neutrophil-intrinsic IFN
408 signaling as a key axis of antitumor immunity and expand the effector landscape of viral-based
409 cancer immunotherapy. Consistent with these observations, our conditional *Ifnar1* deletion
410 models confirm that IFNAR signaling in neutrophils and other myeloid lineages is indispensable
411 for MQ833 efficacy.

412 Loss of IFNAR1 in *Mrp8*$^{+}$ neutrophils, *Cd64*$^{+}$ macrophages, *LysM*$^{+}$ myeloid cells, or *Cd4*$^{+}$ T
413 cells each attenuated tumor regression, underscoring the cooperative requirement for IFNAR
414 signaling across immune compartments. Neutrophil-specific *Ifnar1* deletion (*Mrp8*^{Cre}*Ifnar1*$^{fl/fl}$)
415 impaired tumor control and memory formation, confirming that neutrophil-intrinsic IFNAR
416 signaling contributes to both cytotoxicity and long-term protection. Similarly, macrophage- or T-
417 cell-specific IFNAR loss reduced efficacy, demonstrating that MQ833-induced tumor clearance
418 relies on coordinated IFNAR–STAT2 signaling across innate and adaptive lineages.

419 These results extend classical paradigms of type I IFN immunity. Earlier studies showed that
420 Ifnar1$^{-/-}$ mice fail to reject immunogenic tumors,[33] and that IFNAR signaling in dendritic cells is
421 required for CD8^{+} T-cell cross-priming and tumor rejection,[34,35] while tumor cell–intrinsic
422 IFNAR promotes antigen presentation and immunogenic cell death.[36] Our findings advance this
423 framework by revealing that, during viral immunotherapy, IFNAR signaling in macrophages,
424 neutrophils, and T cells is equally essential for tumor regression and memory formation,
425 highlighting a coordinated innate–adaptive IFN network as the central mechanism of viral-
426 induced antitumor immunity.

427 The abscopal effects of MQ833 underscore its systemic reach. In bilateral tumor models,
428 intratumoral MQ833 reshaped both injected and distant lesions, expanding M1/ISG$^+$
429 macrophages and effector CD8$^+$ T cells while reducing Tregs and M2 macrophages. These
430 results demonstrate that local viral infection propagates systemic immune activation through type
431 I IFN–dependent circuits that synchronize cytotoxic activity across tumor sites.

432 Mechanistically, MQ833 differs from lytic oncolytic viruses such as HSV-1–derived T-VEC [37]
433 or adenovirus CG0070.[38] Whereas T-VEC primarily achieves local tumor lysis and induces
434 regional immune activation with modest systemic effects, MQ833 amplifies cytosolic nucleic
435 acid sensing and IFN-driven myeloid–T-cell cross-talk through rational gene deletions and
436 localized IL-12 expression. This strategy achieves durable systemic immunity with minimal
437 toxicity, exemplifying a paradigm shift from direct oncolysis to immune orchestration.

438 From a translational perspective, MQ833 provides a versatile framework for rational viral
439 design. Its ability to eradicate MHC I–deficient and ICB-resistant tumors highlight myeloid
440 activation as a complementary mechanism of tumor control. Because MVA-based platforms are
441 well-characterized, scalable, and clinically proven to be safe, the design principles established
442 here can be rapidly applied to clinical-grade constructs.

443 In summary, MQ833 is a second-generation recombinant MVA that integrates rational viral
444 engineering with localized cytokine delivery to achieve robust, multifaceted antitumor immunity.
445 By combining deletion of viral immune-evasion genes (*E3L*, *E5R*, *WR199*) with extracellular-
446 matrix-anchored IL-12 expression, MQ833 activates dual MDA5–STING sensing and amplifies
447 STAT2-mediated type I IFN signaling within the tumor microenvironment. These coordinated
448 pathways remodel the myeloid and T-cell compartments, driving recruitment and activation of
449 *Nos2*$^+$ neutrophils and M1-polarized macrophages, depletion of Tregs, and expansion of effector-
450 memory CD8$^+$ T cells.

451 The discovery that myeloid and T cell-intrinsic IFNAR signaling underlies tumor control and
452 antitumor memory redefines the effector architecture of viral immunotherapy, positioning
453 MQ833 as a mechanistically defined and clinically translatable platform for combination
454 immunotherapy.

455 **REFERENCES**

456 1. Binnewies, M., Roberts, E.W., Kersten, K., Chan, V., Fearon, D.F., Merad, M.,
457 Coussens, L.M., Gabrilovich, D.I., Ostrand-Rosenberg, S., Hedrick, C.C., et al. (2018).
458 Understanding the tumor immune microenvironment (TIME) for effective therapy. Nat
459 Med *24*, 541-550. 10.1038/s41591-018-0014-x.
460 2. Tcyganov, E., Mastio, J., Chen, E., and Gabrilovich, D.I. (2018). Plasticity of myeloid-
461 derived suppressor cells in cancer. Curr Opin Immunol *51*, 76-82.
462 10.1016/j.coi.2018.03.009.
463 3. Gajewski, T.F., Schreiber, H., and Fu, Y.X. (2013). Innate and adaptive immune cells in
464 the tumor microenvironment. Nat Immunol *14*, 1014-1022. 10.1038/ni.2703.
465 4. Kim, T.K., Vandsemb, E.N., Herbst, R.S., and Chen, L. (2022). Adaptive immune
466 resistance at the tumour site: mechanisms and therapeutic opportunities. Nat Rev Drug
467 Discov *21*, 529-540. 10.1038/s41573-022-00493-5.
468 5. Kraehenbuehl, L., Weng, C.H., Eghbali, S., Wolchok, J.D., and Merghoub, T. (2022).
469 Enhancing immunotherapy in cancer by targeting emerging immunomodulatory
470 pathways. Nat Rev Clin Oncol *19*, 37-50. 10.1038/s41571-021-00552-7.
471 6. Ribas, A., and Wolchok, J.D. (2018). Cancer immunotherapy using checkpoint blockade.
472 Science *359*, 1350-1355. 10.1126/science.aar4060.
473 7. Zappasodi, R., Merghoub, T., and Wolchok, J.D. (2018). Emerging Concepts for Immune
474 Checkpoint Blockade-Based Combination Therapies. Cancer Cell *34*, 690.
475 10.1016/j.ccell.2018.09.008.
476 8. Melcher, A., Harrington, K., and Vile, R. (2021). Oncolytic virotherapy as
477 immunotherapy. Science *374*, 1325-1326. 10.1126/science.abk3436.
478 9. Russell, S.J., and Barber, G.N. (2018). Oncolytic Viruses as Antigen-Agnostic Cancer
479 Vaccines. Cancer Cell *33*, 599-605. 10.1016/j.ccell.2018.03.011.
480 10. Shalhout, S.Z., Miller, D.M., Emerick, K.S., and Kaufman, H.L. (2023). Therapy with
481 oncolytic viruses: progress and challenges. Nat Rev Clin Oncol *20*, 160-177.
482 10.1038/s41571-022-00719-w.
483 11. DePeaux, K., and Delgoffe, G.M. (2024). Integrating innate and adaptive immunity in
484 oncolytic virus therapy. Trends Cancer *10*, 135-146. 10.1016/j.trecan.2023.09.012.
485 12. Davola, M.E., and Mossman, K.L. (2019). Oncolytic viruses: how "lytic" must they be
486 for therapeutic efficacy? Oncoimmunology *8*, e1581528.
487 10.1080/2162402X.2019.1596006.
488 13. Brown, M.C., Mosaheb, M.M., Mohme, M., McKay, Z.P., Holl, E.K., Kastan, J.P., Yang,
489 Y., Beasley, G.M., Hwang, E.S., Ashley, D.M., et al. (2021). Viral infection of cells
490 within the tumor microenvironment mediates antitumor immunotherapy via selective
491 TBK1-IRF3 signaling. Nat Commun *12*, 1858. 10.1038/s41467-021-22088-1.
492 14. Dai, P., Wang, W., Yang, N., Serna-Tamayo, C., Ricca, J.M., Zamarin, D., Shuman, S.,
493 Merghoub, T., Wolchok, J.D., and Deng, L. (2017). Intratumoral delivery of inactivated
494 modified vaccinia virus Ankara (iMVA) induces systemic antitumor immunity via
495 STING and Batf3-dependent dendritic cells. Sci Immunol *2*.
496 10.1126/sciimmunol.aal1713.
497 15. Wang, W., Liu, S., Dai, P., Yang, N., Wang, Y., Giese, R.A., Merghoub, T., Wolchok, J.,
498 and Deng, L. (2021). Elucidating mechanisms of antitumor immunity mediated by live
499 oncolytic vaccinia and heat-inactivated vaccinia. J Immunother Cancer *9*. 10.1136/jitc-
500 2021-002569.

501 16. Svensson-Arvelund, J., Cuadrado-Castano, S., Pantsulaia, G., Kim, K., Aleynick, M.,
502 Hammerich, L., Upadhyay, R., Yellin, M., Marsh, H., Oreper, D., et al. (2022).
503 Expanding cross-presenting dendritic cells enhances oncolytic virotherapy and is critical
504 for long-term anti-tumor immunity. Nat Commun *13*, 7149. 10.1038/s41467-022-34791-
505 8.
506 17. Stickl, H., and Hochstein-Mintzel, V. (1971). [Intracutaneous smallpox vaccination with
507 a weak pathogenic vaccinia virus ("MVA virus")]. Munch Med Wochenschr *113*, 1149-
508 1153.
509 18. Antoine, G., Scheiflinger, F., Dorner, F., and Falkner, F.G. (1998). The complete
510 genomic sequence of the modified vaccinia Ankara strain: comparison with other
511 orthopoxviruses. Virology *244*, 365-396. 10.1006/viro.1998.9123.
512 19. Pittman, P.R., Hahn, M., Lee, H.S., Koca, C., Samy, N., Schmidt, D., Hornung, J.,
513 Weidenthaler, H., Heery, C.R., Meyer, T.P.H., et al. (2019). Phase 3 Efficacy Trial of
514 Modified Vaccinia Ankara as a Vaccine against Smallpox. N Engl J Med *381*, 1897-
515 1908. 10.1056/NEJMoa1817307.
516 20. Gilbert, S.C. (2013). Clinical development of Modified Vaccinia virus Ankara vaccines.
517 Vaccine *31*, 4241-4246. 10.1016/j.vaccine.2013.03.020.
518 21. Volz, A., and Sutter, G. (2017). Modified Vaccinia Virus Ankara: History, Value in Basic
519 Research, and Current Perspectives for Vaccine Development. Adv Virus Res *97*, 187-
520 243. 10.1016/bs.aivir.2016.07.001.
521 22. Dai, P., Wang, W., Cao, H., Avogadri, F., Dai, L., Drexler, I., Joyce, J.A., Li, X.D.,
522 Chen, Z., Merghoub, T., Shuman, S., and Deng, L. (2014). Modified vaccinia virus
523 Ankara triggers type I IFN production in murine conventional dendritic cells via a
524 cGAS/STING-mediated cytosolic DNA-sensing pathway. PLoS Pathog *10*, e1003989.
525 10.1371/journal.ppat.1003989.
526 23. Yang, N., Wang, Y., Liu, S., Luna, J.M., Mazo, G., Tan, A.Y., Zhang, T., Wang, J., Yan,
527 W., Choi, J., et al. (2021). Intratumoral delivery of engineered recombinant modified
528 vaccinia virus Ankara expressing Flt3L and OX40L generates potent antitumor immunity
529 through activating the cGAS/STING pathway and depleting tumor-infiltrating regulatory
530 T cells. bioRxiv, 2021.2010.2031.466698. 10.1101/2021.10.31.466698.
531 24. Deng, L., Dai, P., Ding, W., Granstein, R.D., and Shuman, S. (2006). Vaccinia virus
532 infection attenuates innate immune responses and antigen presentation by epidermal
533 dendritic cells. J Virol *80*, 9977-9987. 10.1128/JVI.00354-06.
534 25. Deng, L., Dai, P., Parikh, T., Cao, H., Bhoj, V., Sun, Q., Chen, Z., Merghoub, T.,
535 Houghton, A., and Shuman, S. (2008). Vaccinia virus subverts a mitochondrial antiviral
536 signaling protein-dependent innate immune response in keratinocytes through its double-
537 stranded RNA binding protein, E3. J Virol *82*, 10735-10746. 10.1128/JVI.01305-08.
538 26. Yang, N., Wang, Y., Dai, P., Li, T., Zierhut, C., Tan, A., Zhang, T., Xiang, J.Z.,
539 Ordureau, A., Funabiki, H., Chen, Z., and Deng, L. (2023). Vaccinia E5 is a major
540 inhibitor of the DNA sensor cGAS. Nat Commun *14*, 2898. 10.1038/s41467-023-38514-
541 5.
542 27. Yang, N., Wang, Y., Dai, P., Li, T., Zierhut, C., Tan, A., Zhang, T., Pan, H., Li, Z.,
543 Ordureau, A., et al. (2021). Vaccinia E5 is a major inhibitor of the DNA sensor cGAS.
544 bioRxiv, 2021.2010.2025.465197. 10.1101/2021.10.25.465197.
545 28. Wyatt, L.S., Shors, S.T., Murphy, B.R., and Moss, B. (1996). Development of a
546 replication-deficient recombinant vaccinia virus vaccine effective against parainfluenza

547 virus 3 infection in an animal model. Vaccine *14*, 1451-1458. 10.1016/s0264-
548 410x(96)00072-2.
549 29. Bisht, H., Roberts, A., Vogel, L., Bukreyev, A., Collins, P.L., Murphy, B.R., Subbarao,
550 K., and Moss, B. (2004). Severe acute respiratory syndrome coronavirus spike protein
551 expressed by attenuated vaccinia virus protectively immunizes mice. Proc Natl Acad Sci
552 U S A *101*, 6641-6646. 10.1073/pnas.0401939101.
553 30. Benguigui, M., Cooper, T.J., Kalkar, P., Schif-Zuck, S., Halaban, R., Bacchiocchi, A.,
554 Kamer, I., Deo, A., Manobla, B., Menachem, R., et al. (2024). Interferon-stimulated
555 neutrophils as a predictor of immunotherapy response. Cancer Cell *42*, 253-265 e212.
556 10.1016/j.ccell.2023.12.005.
557 31. Hirschhorn, D., Budhu, S., Kraehenbuehl, L., Gigoux, M., Schroder, D., Chow, A.,
558 Ricca, J.M., Gasmi, B., De Henau, O., Mangarin, L.M.B., et al. (2023). T cell
559 immunotherapies engage neutrophils to eliminate tumor antigen escape variants. Cell
560 *186*, 1432-1447 e1417. 10.1016/j.cell.2023.03.007.
561 32. Gungabeesoon, J., Gort-Freitas, N.A., Kiss, M., Bolli, E., Messemaker, M., Siwicki, M.,
562 Hicham, M., Bill, R., Koch, P., Cianciaruso, C., et al. (2023). A neutrophil response
563 linked to tumor control in immunotherapy. Cell *186*, 1448-1464 e1420.
564 10.1016/j.cell.2023.02.032.
565 33. Dunn, G.P., Bruce, A.T., Sheehan, K.C., Shankaran, V., Uppaluri, R., Bui, J.D.,
566 Diamond, M.S., Koebel, C.M., Arthur, C., White, J.M., and Schreiber, R.D. (2005). A
567 critical function for type I interferons in cancer immunoediting. Nat Immunol *6*, 722-729.
568 10.1038/ni1213.
569 34. Fuertes, M.B., Kacha, A.K., Kline, J., Woo, S.R., Kranz, D.M., Murphy, K.M., and
570 Gajewski, T.F. (2011). Host type I IFN signals are required for antitumor CD8+ T cell
571 responses through CD8alpha+ dendritic cells. J Exp Med *208*, 2005-2016.
572 10.1084/jem.20101159.
573 35. Diamond, M.S., Kinder, M., Matsushita, H., Mashayekhi, M., Dunn, G.P., Archambault,
574 J.M., Lee, H., Arthur, C.D., White, J.M., Kalinke, U., Murphy, K.M., and Schreiber, R.D.
575 (2011). Type I interferon is selectively required by dendritic cells for immune rejection of
576 tumors. J Exp Med *208*, 1989-2003. 10.1084/jem.20101158.
577 36. Sistigu, A., Yamazaki, T., Vacchelli, E., Chaba, K., Enot, D.P., Adam, J., Vitale, I.,
578 Goubar, A., Baracco, E.E., Remedios, C., et al. (2014). Cancer cell-autonomous
579 contribution of type I interferon signaling to the efficacy of chemotherapy. Nat Med *20*,
580 1301-1309. 10.1038/nm.3708.
581 37. Andtbacka, R.H., Kaufman, H.L., Collichio, F., Amatruda, T., Senzer, N., Chesney, J.,
582 Delman, K.A., Spitler, L.E., Puzanov, I., Agarwala, S.S., et al. (2015). Talimogene
583 Laherparepvec Improves Durable Response Rate in Patients With Advanced Melanoma.
584 J Clin Oncol *33*, 2780-2788. 10.1200/JCO.2014.58.3377.
585 38. Packiam, V.T., Lamm, D.L., Barocas, D.A., Trainer, A., Fand, B., Davis, R.L., 3rd,
586 Clark, W., Kroeger, M., Dumbadze, I., Chamie, K., et al. (2018). An open label, single-
587 arm, phase II multicenter study of the safety and efficacy of CG0070 oncolytic vector
588 regimen in patients with BCG-unresponsive non-muscle-invasive bladder cancer: Interim
589 results. Urol Oncol *36*, 440-447. 10.1016/j.urolonc.2017.07.005.
590 39. Sauer, J.D., Sotelo-Troha, K., von Moltke, J., Monroe, K.M., Rae, C.S., Brubaker, S.W.,
591 Hyodo, M., Hayakawa, Y., Woodward, J.J., Portnoy, D.A., and Vance, R.E. (2011). The
592 N-ethyl-N-nitrosourea-induced Goldenticket mouse mutant reveals an essential function

593 of Sting in the in vivo interferon response to Listeria monocytogenes and cyclic
594 dinucleotides. Infect Immun *79*, 688-694. 10.1128/IAI.00999-10.
595 40. Schoggins, J.W., MacDuff, D.A., Imanaka, N., Gainey, M.D., Shrestha, B., Eitson, J.L.,
596 Mar, K.B., Richardson, R.B., Ratushny, A.V., Litvak, V., et al. (2014). Pan-viral
597 specificity of IFN-induced genes reveals new roles for cGAS in innate immunity. Nature
598 *505*, 691-695. 10.1038/nature12862.
599 41. Park, C., Li, S., Cha, E., and Schindler, C. (2000). Immune response in Stat2 knockout
600 mice. Immunity *13*, 795-804. 10.1016/s1074-7613(00)00077-7.
601 42. Laubach, V.E., Shesely, E.G., Smithies, O., and Sherman, P.A. (1995). Mice lacking
602 inducible nitric oxide synthase are not resistant to lipopolysaccharide-induced death. Proc
603 Natl Acad Sci U S A *92*, 10688-10692. 10.1073/pnas.92.23.10688.
604 43. Gitlin, L., Barchet, W., Gilfillan, S., Cella, M., Beutler, B., Flavell, R.A., Diamond, M.S.,
605 and Colonna, M. (2006). Essential role of mda-5 in type I IFN responses to
606 polyriboinosinic:polyribocytidylic acid and encephalomyocarditis picornavirus. Proc Natl
607 Acad Sci U S A *103*, 8459-8464. 10.1073/pnas.0603082103.
608 44. Yang, N., Luna, J.M., Dai, P., Wang, Y., Rice, C.M., and Deng, L. (2022). Lung type II
609 alveolar epithelial cells collaborate with CCR2(+) inflammatory monocytes in host
610 defense against poxvirus infection. Nat Commun *13*, 1671. 10.1038/s41467-022-29308-
611 2.
612 45. Zhang, X., Li, S., Malik, I., Do, M.H., Ji, L., Chou, C., Shi, W., Capistrano, K.J., Zhang,
613 J., Hsu, T.W., et al. (2023). Reprogramming tumour-associated macrophages to
614 outcompete cancer cells. Nature *619*, 616-623. 10.1038/s41586-023-06256-5.
615 46. Clausen, B.E., Burkhardt, C., Reith, W., Renkawitz, R., and Forster, I. (1999).
616 Conditional gene targeting in macrophages and granulocytes using LysMcre mice.
617 Transgenic Res *8*, 265-277. 10.1023/a:1008942828960.
618 47. Sawada, S., Scarborough, J.D., Killeen, N., and Littman, D.R. (1994). A lineage-specific
619 transcriptional silencer regulates CD4 gene expression during T lymphocyte
620 development. Cell *77*, 917-929. 10.1016/0092-8674(94)90140-6.
621 48. Subramanian, A., Tamayo, P., Mootha, V.K., Mukherjee, S., Ebert, B.L., Gillette, M.A.,
622 Paulovich, A., Pomeroy, S.L., Golub, T.R., Lander, E.S., and Mesirov, J.P. (2005). Gene
623 set enrichment analysis: a knowledge-based approach for interpreting genome-wide
624 expression profiles. Proc Natl Acad Sci U S A *102*, 15545-15550.
625 10.1073/pnas.0506580102.
626

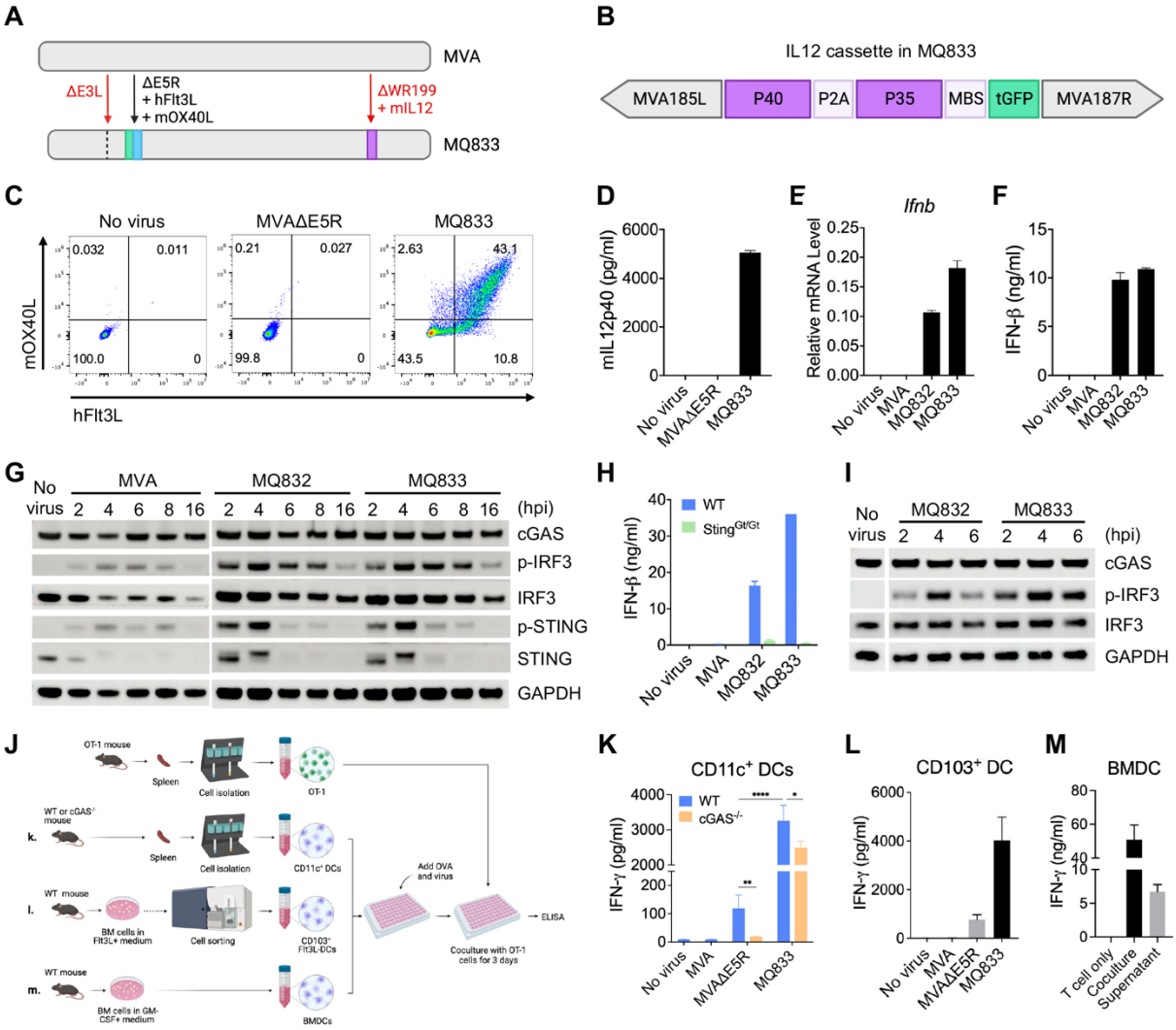
A
MVA
ΔE3L
ΔE5R
+ hFlt3L
+ mOX40L
ΔWR199
+ mIL12
MQ833
B
IL12 cassette in MQ833
MVA185L
P40
P2A
P35
MBS
tGFP
MVA187R
C
No virus
MVAΔE5R
MQ833
mOX40L
hFlt3L
0.032
0.011
100.0
0
0.21
0.027
99.8
0
2.63
43.1
43.5
10.8
D
mIL12p40 (pg/ml)
No virus
MVAΔE5R
MQ833
E
Ifnb
Relative mRNA Level
No virus
MVA
MQ832
MQ833
F
IFN-β (ng/ml)
No virus
MVA
MQ832
MQ833
G
No virus
MVA
MQ832
MQ833
(hpi)
cGAS
p-IRF3
IRF3
p-STING
STING
GAPDH
H
WT
Sting^Gt/Gt
IFN-β (ng/ml)
No virus
MVA
MQ832
MQ833
I
No virus
MQ832
MQ833
(hpi)
cGAS
p-IRF3
IRF3
GAPDH
J
OT-1 mouse
Spleen
Cell isolation
OT-1
WT or cGAS-/- mouse
CD11c+ DCs
WT mouse
BM cells in Flt3L+ medium
Cell sorting
CD103+ Flt3L-DCs
BM cells in GM-CSF+ medium
BMDCs
Add OVA and virus
Coculture with OT-1 cells for 3 days
ELISA
K
CD11c+ DCs
WT
cGAS-/-
IFN-γ (pg/ml)
No virus
MVA
MVAΔE5R
MQ833
L
CD103+ DC
IFN-γ (pg/ml)
No virus
MVA
MVAΔE5R
MQ833
M
BMDC
IFN-γ (ng/ml)
T cell only
Coculture
Supernatant

627 **Figure 1. MQ833 infection of tumor and immune cells activates cGAS/STING mediated**
628 **dsDNA sensing pathway and promotes IFN production**
629 (A) Schematic of MQ833 design showing sequential deletions of viral immune-evasion genes
630 (*E5R*, *E3L*, *WR199*) and insertion of transgenes encoding hFlt3L, mOX40L, and extracellular
631 matrix-anchored mIL-12.
632 (B) Diagram of the bicistronic IL-12 cassette (Il12a–P2A–Il12b) integrated into the *WR199*
633 locus.
634 (C and D) B16-F10 tumor cells infected with MVAΔE5R or MQ833 (MOI = 10) for 16 h. (C)
635 Flow cytometry showing surface expression of hFlt3L and mOX40L. (D) ELISA quantifying
636 secreted mIL-12p40.
637 (E and F) B16-F10 tumor cells infected with indicated viruses (MOI = 10) for 16 h. qRT-PCR
638 and ELISA showing increased *Ifnb* transcripts (E) and IFN-β secretion (F) in MQ833-infected
639 cells versus controls.
640 (G) Western blot analysis of cGAS/STING pathway activation in B16-F10 cells infected with
641 indicated viruses (MOI = 10) and collected at 2–16 h post-infection (hpi).
642 (H and I) BMDCs from WT or $Sting^{Gt/Gt}$ mice infected (MOI = 10). (H) ELISA quantification of
643 IFN-β secretion. (I) Western blot for cGAS, p-IRF3, and IRF3.
644 (J) Experimental schematic of DC–T-cell coculture used to evaluate antigen cross-presentation.
645 (K–M) ELISA quantification of IFN-γ in supernatants from OT-I T-cell cocultures. (K) Splenic
646 $CD11c^{+}$ DCs from WT or $cGAS^{-/-}$ mice pulsed with OVA and infected with indicated viruses.
647 (L) Sorted $CD103^{+}$ DCs from Flt3L-expanded cultures pulsed with OVA and infected as in (K).
648 (M) Comparison of OT-I activation using direct coculture versus conditioned medium from
649 MQ833-infected BMDCs, showing contact-dependent T-cell stimulation. Data are representative
650 of ≥ 2 independent experiments.

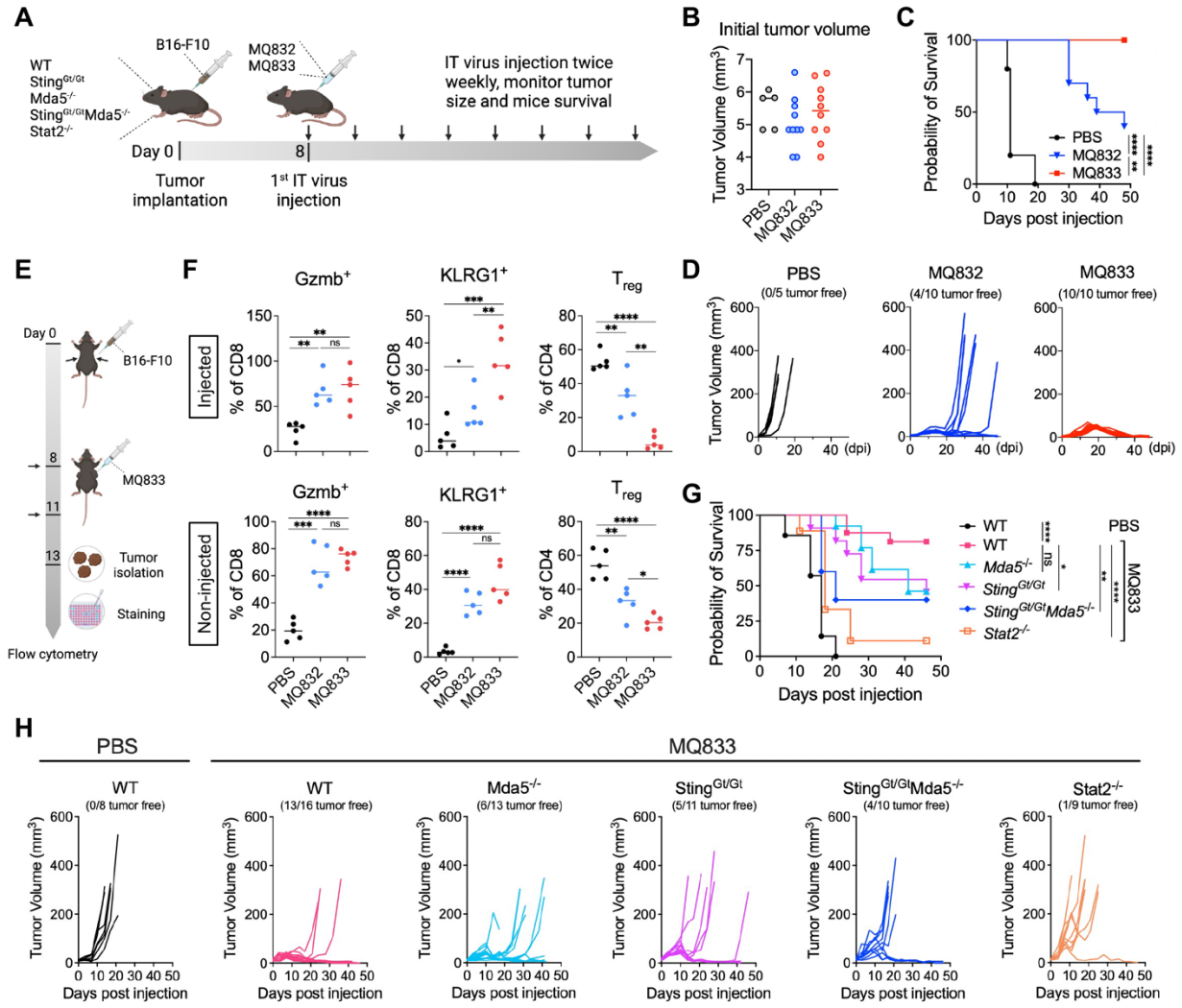
A
WT
Sting$^{Gt/Gt}$
Mda5$^{-/-}$
Sting$^{Gt/Gt}$Mda5$^{-/-}$
Stat2$^{-/-}$
B16-F10
MQ832
MQ833
IT virus injection twice weekly, monitor tumor size and mice survival
Day 0
8
Tumor implantation
1st IT virus injection
B
Initial tumor volume
Tumor Volume (mm^3)
PBS
MQ832
MQ833
C
Probability of Survival
Days post injection
PBS
MQ832
MQ833
E
Day 0
B16-F10
8
MQ833
11
13
Tumor isolation
Staining
Flow cytometry
F
Gzmb$^+$
KLRG1$^+$
T$_{reg}$
Injected
Non-injected
% of CD8
% of CD4
PBS
MQ832
MQ833
D
PBS
(0/5 tumor free)
MQ832
(4/10 tumor free)
MQ833
(10/10 tumor free)
Tumor Volume (mm^3)
(dpi)
G
Probability of Survival
Days post injection
WT
WT
Mda5$^{-/-}$
Sting$^{Gt/Gt}$
Sting$^{Gt/Gt}$Mda5$^{-/-}$
Stat2$^{-/-}$
PBS
MQ833
H
PBS
MQ833
WT
(0/8 tumor free)
WT
(13/16 tumor free)
Mda5$^{-/-}$
(6/13 tumor free)
Sting$^{Gt/Gt}$
(5/11 tumor free)
Sting$^{Gt/Gt}$Mda5$^{-/-}$
(4/10 tumor free)
Stat2$^{-/-}$
(1/9 tumor free)
Tumor Volume (mm^3)
Days post injection

651 **Figure 2. Intratumoral (IT) delivery of MQ833 generates an 80-100% cure in B16-F10**
652 **melanoma model in a STING-MDA5-STAT2-dependent manner**
653 (A) Schematic diagram of survival experiment.
654 (B) Kaplan-Meier survival curve of B16-F10 tumor bearing mice treated with MQ833. PBS was
655 used as a control. (n=5-10) Survival data were analyzed by log-rank (Mantel-Cox) test.
656 (*$^{**}P<0.01$, $^{****}P < 0.0001$*) .
657 (C) Initial tumor volume for each group.
658 (D) Tumor volumes of mice injected with MQ832, MQ833 or PBS over days post treatment.
659 (E) Schematic diagram of flow cytometric analysis of tumor infiltrating lymphocytes.
660 (F) Percentage of specific cell population in the injected and non-injected tumors in different
661 treatment groups.
662 (G) Kaplan-Meier survival curve of B16-F10 tumor bearing mice treated with MQ833. PBS was
663 used as a control. Survival data were analyzed by log-rank (Mantel-Cox) test. (n=5; *$^{*}P<0.05$,
664 $^{**}P<0.01$, $^{****}P < 0.0001$, *t test*).
665 (H) Tumor volume curves in different groups over days post treatment.

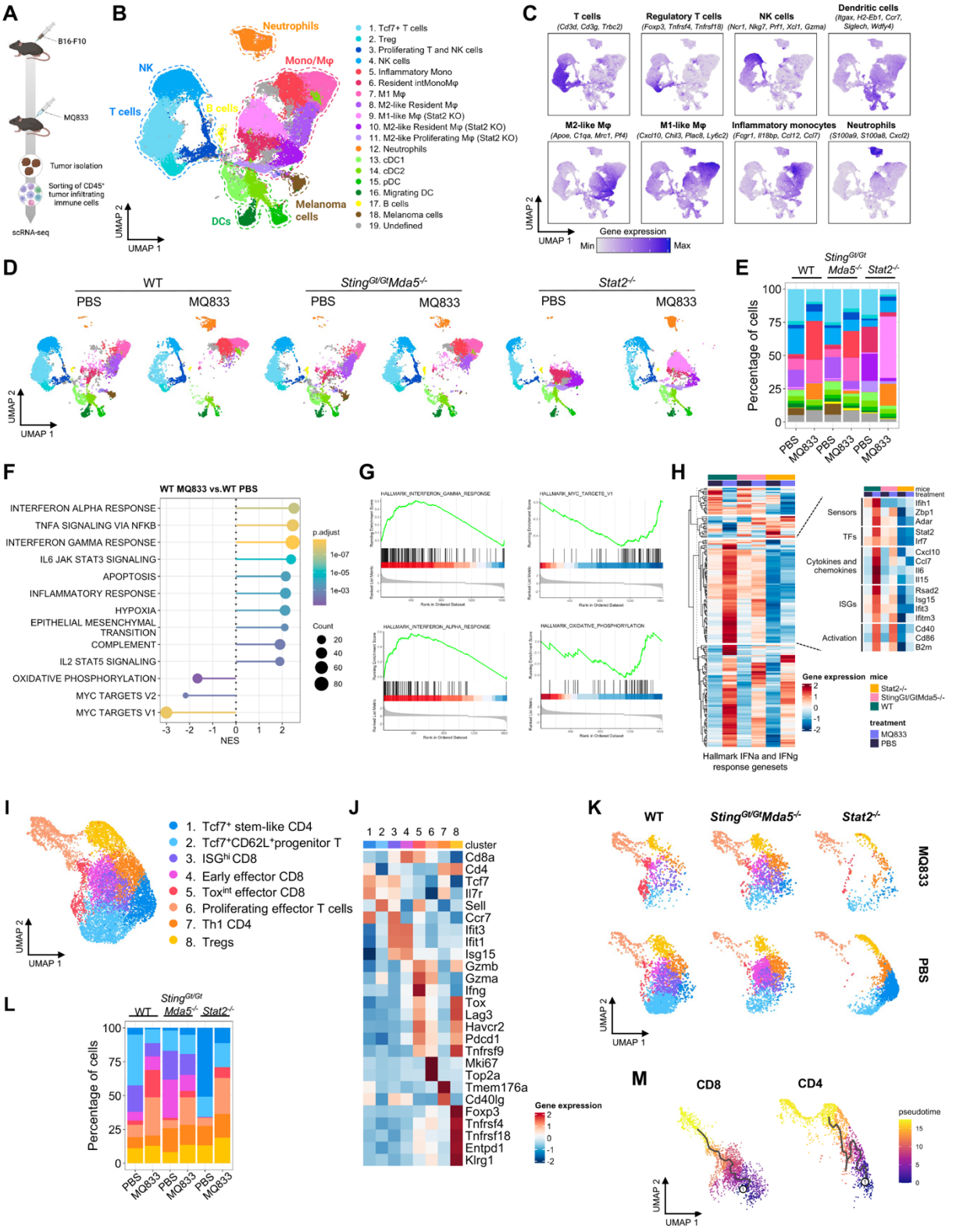
A
B16-F10
MQ833
Tumor isolation
Sorting of CD45+ tumor infiltrating immune cells
scRNA-seq
B
Neutrophils
Mono/Mφ
NK
T cells
B cells
DCs
Melanoma cells
UMAP 2
UMAP 1
1. Tcf7+ T cells
2. Treg
3. Proliferating T and NK cells
4. NK cells
5. Inflammatory Mono
6. Resident intMonoMφ
7. M1 Mφ
8. M2-like Resident Mφ
9. M1-like Mφ (Stat2 KO)
10. M2-like Resident Mφ (Stat2 KO)
11. M2-like Proliferating Mφ (Stat2 KO)
12. Neutrophils
13. cDC1
14. cDC2
15. pDC
16. Migrating DC
17. B cells
18. Melanoma cells
19. Undefined
C
T cells (Cd3d, Cd3g, Trbc2)
Regulatory T cells (Foxp3, Tnfrsf4, Tnfrsf18)
NK cells (Ncr1, Nkg7, Prf1, Xcl1, Gzma)
Dendritic cells (Itgax, H2-Eb1, Ccr7, Siglech, Wdfy4)
M2-like Mφ (Apoe, C1qa, Mrc1, Pf4)
M1-like Mφ (Cxcl10, Chil3, Plac8, Ly6c2)
Inflammatory monocytes (Fcgr1, Il18bp, Ccl12, Ccl7)
Neutrophils (S100a9, S100a8, Cxcl2)
Gene expression
Min
Max
D
WT
PBS
MQ833
Sting Gt/Gt Mda5-/-
Stat2-/-
E
Percentage of cells
F
WT MQ833 vs.WT PBS
INTERFERON ALPHA RESPONSE
TNFA SIGNALING VIA NFKB
INTERFERON GAMMA RESPONSE
IL6 JAK STAT3 SIGNALING
APOPTOSIS
INFLAMMATORY RESPONSE
HYPOXIA
EPITHELIAL MESENCHYMAL TRANSITION
COMPLEMENT
IL2 STAT5 SIGNALING
OXIDATIVE PHOSPHORYLATION
MYC TARGETS V2
MYC TARGETS V1
NES
p.adjust
Count
G
HALLMARK_INTERFERON_GAMMA_RESPONSE
HALLMARK_MYC_TARGETS_V1
HALLMARK_INTERFERON_ALPHA_RESPONSE
HALLMARK_OXIDATIVE_PHOSPHORYLATION
H
Sensors
TFs
Cytokines and chemokines
ISGs
Activation
Ifih1
Zbp1
Adar
Stat2
Irf7
Cxcl10
Ccl7
Il6
Il15
Rsad2
Isg15
Ifit3
Ifitm3
Cd40
Cd86
B2m
Gene expression
mice
Stat2-/-
StingGt/GtMda5-/-
WT
treatment
MQ833
PBS
Hallmark IFNa and IFNg response genesets
I
1. Tcf7+ stem-like CD4
2. Tcf7+CD62L+progenitor T
3. ISGhi CD8
4. Early effector CD8
5. Toxint effector CD8
6. Proliferating effector T cells
7. Th1 CD4
8. Tregs
J
cluster
Cd8a
Cd4
Tcf7
Il7r
Sell
Ccr7
Ifit3
Ifit1
Isg15
Gzmb
Gzma
Ifng
Tox
Lag3
Havcr2
Pdcd1
Tnfrsf9
Mki67
Top2a
Tmem176a
Cd40lg
Foxp3
Tnfrsf4
Tnfrsf18
Entpd1
Klrg1
Gene expression
K
WT
Sting Gt/Gt Mda5-/-
Stat2-/-
MQ833
PBS
L
Percentage of cells
M
CD8
CD4
pseudotime

666 **Figure 3. IT MQ833 treatment reprograms the tumor-infiltrated immune cells**

667 (A) Schematic diagram of the experimental schedule.

668 (B) UMAP display of sorted $CD45^+$ cells from 6 samples combined following 10X Genomics
669 scRNA-seq workflow (n = 47020 cells).

670 (C) Expression plots of 8 main cell types using their top marker genes.

671 (D) UMAP plots of cell clusters separated by sample.

672 (E) Stacked bar plot showing the percentage of each cluster across different samples.

673 (F) Dot plot for the top enriched and suppressed gene sets from the Molecular Signature
674 Database (MSigDB) Hallmark immunologic signature gene sets in WT MQ833 versus WT PBS.

675 (G) Gene set enrichment analysis (GSEA) for individual pathways from the representative
676 enriched and suppressed gene sets in WT MQ833 sample compared with WT PBS.

677 (H) Heatmaps of the average expression of genes in the hallmark IFNα and IFNγ response gene
678 sets. Selected genes of interest are labeled in the right panel.

679 (I) UMAP display of subclustered *Cd3e*$^+$ cells from 6 samples combined following 10X
680 Genomics scRNA-seq workflow (n = 9,540 cells).

681 (J) Cluster-defining marker expression was visualized in a heatmap. T cell subclusters includes
682 $Tcf7^+$ stem-like CD4 T cells (*Tcf7, Il7r, Cd4*), $Tcf7^+CD62L^+$ progenitor T cells (*Tcf7, Il7r, Sell*),
683 ISG^{hi} CD8 T cells (*Tcf7, Ccr7, Ifit1, Ifit3, Isg15*), early effector $CD8^+$ T cells (*Isg15, Ifit3, Gzmb,*
684 *Ifng*), Tox^{int} effector $CD8^+$ T cells (*Gzmb*^{hi}*, Gzma*^{hi}*, Ifng*^{hi}), proliferating effector $CD8^+$ T cells
685 (*Mki67* and *Top2a)*. Th1 $CD4^+$ T-cell (*Cd4, Il7r, Tmem176a*, *Cd40lg)*, and regulatory T cells
686 (Tregs), marked by CD4, *Foxp3, Tnfrsf4* (OX40), *Tnfrsf18* (GITR), *Entpd1, Klrg1* expression.

687 (K) UMAP plots of cell clusters separated by sample.

688 (L) Stacked bar plot showing the percentage of each cluster across different samples.

689 (M) Cell trajectory analysis of CD8 and CD4 T cells.

690

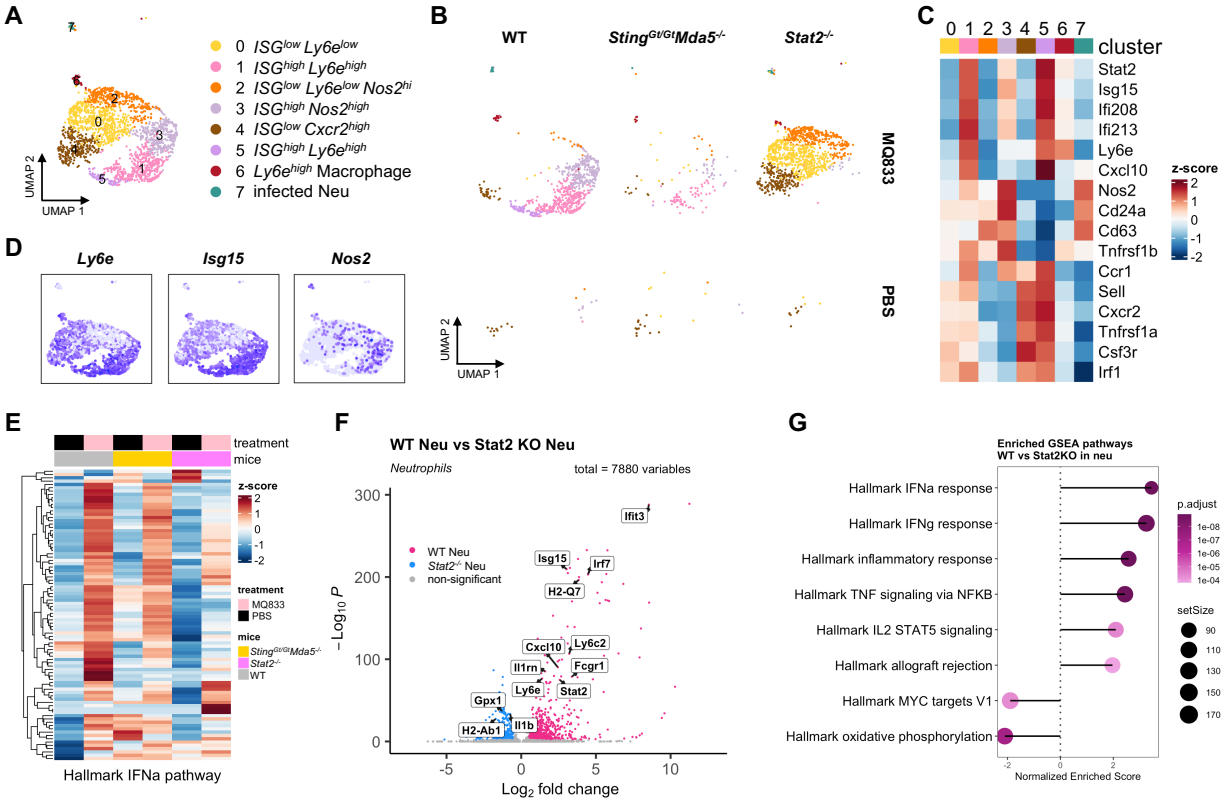
A
0 ISG^low Ly6e^low
1 ISG^high Ly6e^high
2 ISG^low Ly6e^low Nos2^hi
3 ISG^high Nos2^high
4 ISG^low Cxcr2^high
5 ISG^high Ly6e^high
6 Ly6e^high Macrophage
7 infected Neu
UMAP 2
UMAP 1
B
WT
Sting^Gt/Gt Mda5^-/-
Stat2^-/-
MQ833
PBS
C
cluster
Stat2
Isg15
Ifi208
Ifi213
Ly6e
Cxcl10
Nos2
Cd24a
Cd63
Tnfrsf1b
Ccr1
Sell
Cxcr2
Tnfrsf1a
Csf3r
Irf1
z-score
D
Ly6e
Isg15
Nos2
E
treatment
mice
z-score
MQ833
PBS
Hallmark IFNa pathway
F
WT Neu vs Stat2 KO Neu
Neutrophils
total = 7880 variables
WT Neu
Stat2^-/- Neu
non-significant
Ifit3
Isg15
Irf7
H2-Q7
Cxcl10
Ly6c2
Il1rn
Fcgr1
Ly6e
Stat2
Gpx1
H2-Ab1
Il1b
−Log10 P
Log2 fold change
G
Enriched GSEA pathways
WT vs Stat2KO in neu
Hallmark IFNa response
Hallmark IFNg response
Hallmark inflammatory response
Hallmark TNF signaling via NFKB
Hallmark IL2 STAT5 signaling
Hallmark allograft rejection
Hallmark MYC targets V1
Hallmark oxidative phosphorylation
p.adjust
setSize
Normalized Enriched Score

691 **Figure 4. MQ833-induced type I IFN reprograms the tumor-infiltrating neutrophils**

692 (A) UMAP display of subclustered neutrophils (cluster12 in figure. 3B) from 6 samples
693 combined (n = 2,205 cells).

694 (B) UMAP plots of cell clusters separated by sample.

695 (C) Heatmap showing the expression of selected genes across different clusters.

696 (D) Expression plots of *Ly6e*, *Isg15*, and *Nos2*.

697 (E) Heatmaps of the average expression of genes in the hallmark IFNα response gene set.

698 (F) Volcano plots comparing differentially expressed genes in neutrophils in WT and *Stat2*$^{-/-}$
699 mice.

700 (G) Dot plot for the top enriched and suppressed gene sets from the Molecular Signature
701 Database (MSigDB) Hallmark immunologic signature gene sets in MQ833-treated WT mice vs
702 *Stat2*$^{-/-}$ mice.

703

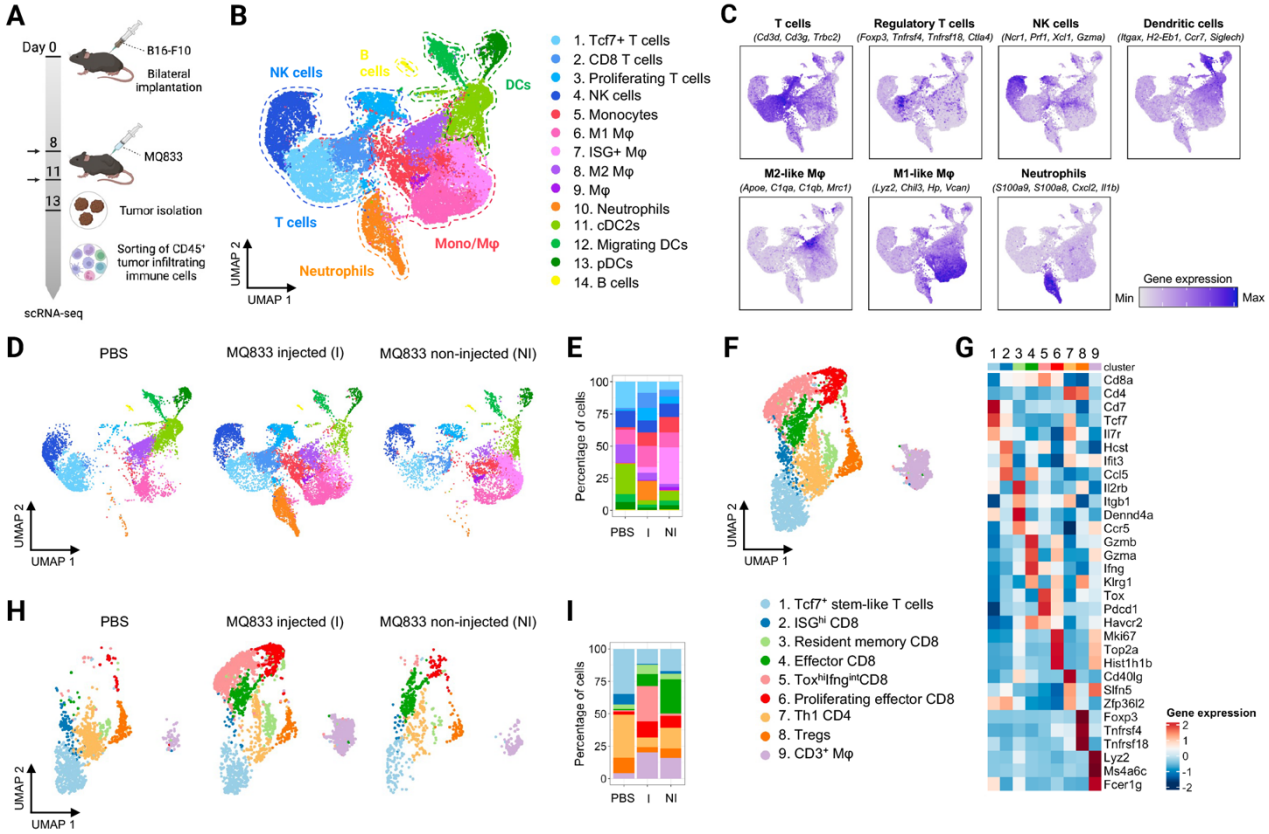
A
Day 0
B16-F10
Bilateral implantation
8
11
13
MQ833
Tumor isolation
Sorting of CD45+ tumor infiltrating immune cells
scRNA-seq
B
NK cells
B cells
DCs
T cells
Mono/Mφ
Neutrophils
UMAP 2
UMAP 1
1. Tcf7+ T cells
2. CD8 T cells
3. Proliferating T cells
4. NK cells
5. Monocytes
6. M1 Mφ
7. ISG+ Mφ
8. M2 Mφ
9. Mφ
10. Neutrophils
11. cDC2s
12. Migrating DCs
13. pDCs
14. B cells
C
T cells
(Cd3d, Cd3g, Trbc2)
Regulatory T cells
(Foxp3, Tnfrsf4, Tnfrsf18, Ctla4)
NK cells
(Ncr1, Prf1, Xcl1, Gzma)
Dendritic cells
(Itgax, H2-Eb1, Ccr7, Siglech)
M2-like Mφ
(Apoe, C1qa, C1qb, Mrc1)
M1-like Mφ
(Lyz2, Chil3, Hp, Vcan)
Neutrophils
(S100a9, S100a8, Cxcl2, Il1b)
Gene expression
Min
Max
D
PBS
MQ833 injected (I)
MQ833 non-injected (NI)
UMAP 2
UMAP 1
E
Percentage of cells
100
75
50
25
0
PBS
I
NI
F
UMAP 2
UMAP 1
1. Tcf7+ stem-like T cells
2. ISGhi CD8
3. Resident memory CD8
4. Effector CD8
5. Toxhi Ifngint CD8
6. Proliferating effector CD8
7. Th1 CD4
8. Tregs
9. CD3+ Mφ
G
1 2 3 4 5 6 7 8 9
cluster
Cd8a
Cd4
Cd7
Tcf7
Il7r
Hcst
Ifit3
Ccl5
Il2rb
Itgb1
Dennd4a
Ccr5
Gzmb
Gzma
Ifng
Klrg1
Tox
Pdcd1
Havcr2
Mki67
Top2a
Hist1h1b
Cd40lg
Slfn5
Zfp36l2
Foxp3
Tnfrsf4
Tnfrsf18
Lyz2
Ms4a6c
Fcer1g
Gene expression
2
1
0
-1
-2
H
PBS
MQ833 injected (I)
MQ833 non-injected (NI)
UMAP 2
UMAP 1
I
Percentage of cells
100
75
50
25
0
PBS
I
NI

704 **Figure 5. IT MQ833 reprograms TIME in both injected and non-injected tumors in a**
705 **bilateral B16-F10 melanoma model**
706 (A) Schematic diagram of the experimental schedule.
707 (B) UMAP display of sorted $CD45^+$ cells from 3 samples combined following 10X Genomics
708 scRNA-seq workflow (n = 21,675 cells).
709 (C) Expression plots of 7 main cell types using their top marker genes.
710 (D) UMAP plots of cell clusters separated by sample.
711 (E) Stacked bar plot showing the percentage of each cluster across different samples.
712 (F) UMAP display of subclustered *Cd3e*$^+$ cells from 6 samples combined following 10X
713 Genomics scRNA-seq workflow (n = 4,901 cells).
714 (G) Heatmaps of the average expression of representative marker genes for each cluster.
715 (H) UMAP plots of cell clusters separated by sample.
716 (I) Stacked bar plot showing the percentage of each cluster across different samples.

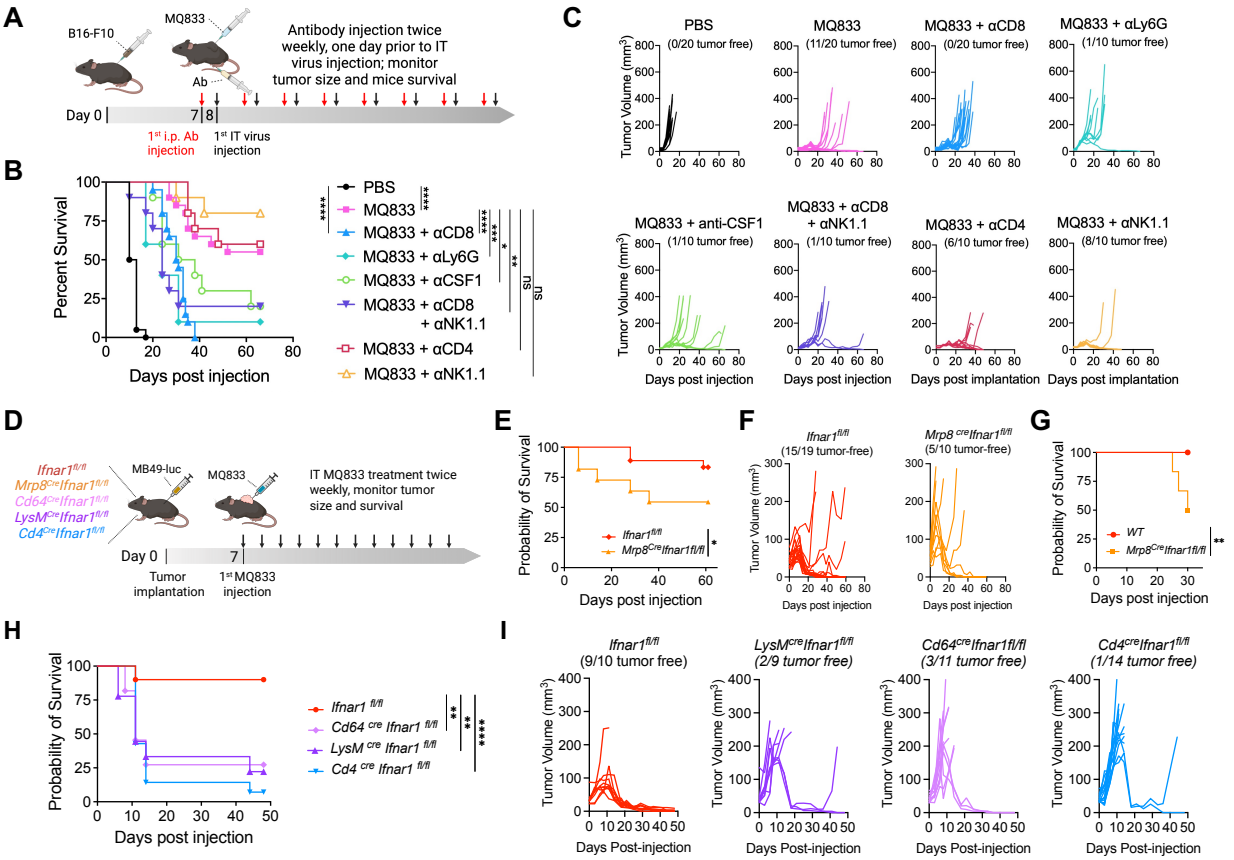
A
B16-F10
MQ833
Ab
Antibody injection twice weekly, one day prior to IT virus injection; monitor tumor size and mice survival
Day 0
7
8
1st i.p. Ab injection
1st IT virus injection
B
Percent Survival
Days post injection
PBS
MQ833
MQ833 + αCD8
MQ833 + αLy6G
MQ833 + αCSF1
MQ833 + αCD8 + αNK1.1
MQ833 + αCD4
MQ833 + αNK1.1
C
PBS (0/20 tumor free)
MQ833 (11/20 tumor free)
MQ833 + αCD8 (0/20 tumor free)
MQ833 + αLy6G (1/10 tumor free)
MQ833 + anti-CSF1 (1/10 tumor free)
MQ833 + αCD8 + αNK1.1 (1/10 tumor free)
MQ833 + αCD4 (6/10 tumor free)
MQ833 + αNK1.1 (8/10 tumor free)
Tumor Volume (mm3)
Days post injection
Days post implantation
D
Ifnar1fl/fl
Mrp8CreIfnar1fl/fl
Cd64CreIfnar1fl/fl
LysMCreIfnar1fl/fl
Cd4CreIfnar1fl/fl
MB49-luc
MQ833
IT MQ833 treatment twice weekly, monitor tumor size and survival
Day 0
7
Tumor implantation
1st MQ833 injection
E
Probability of Survival
Ifnar1fl/fl
Mrp8CreIfnar1fl/fl
Days post injection
F
Ifnar1fl/fl (15/19 tumor-free)
Mrp8 creIfnar1fl/fl (5/10 tumor-free)
Tumor Volume (mm3)
Days post injection
G
Probability of Survival
WT
Mrp8CreIfnar1fl/fl
Days post injection
H
Probability of Survival
Ifnar1 fl/fl
Cd64 cre Ifnar1 fl/fl
LysM cre Ifnar1 fl/fl
Cd4 cre Ifnar1 fl/fl
Days post injection
I
Ifnar1fl/fl (9/10 tumor free)
LysMcreIfnar1fl/fl (2/9 tumor free)
Cd64creIfnar1fl/fl (3/11 tumor free)
Cd4creIfnar1fl/fl (1/14 tumor free)
Tumor Volume (mm3)
Days Post-injection

717 **Figure 6. IFNAR signaling in both T cells and myeloid cells are important for the**
718 **antitumor effects of MQ833**
719 (A) Schematic diagram of the experimental schedule.
720 (B) Kaplan-Meier survival curve of mice in each treatment group. (n=10) Survival data were
721 analyzed by log-rank (Mantel-Cox) test. (n=10-20; $*P < 0.05$, $**P < 0.01$, $****P < 0.0001$).
722 (C) Tumor volumes of mice separated by group over days post treatment.
723 (D) Schematic diagram of the experimental schedule.
724 (E) Kaplan-Meier survival curve of *Ifnar1*$^{fl/fl}$ and *Mrp8*^{Cre}*Ifnar1*$^{fl/fl}$ mice. Survival data were
725 analyzed by log-rank (Mantel-Cox) test. (n=10-19; $*P < 0.05$).
726 (F) Tumor volumes separated by group over days post treatment.
727 (G) Kaplan-Meier survival curve of rechallenged mice in each group. Survival data were
728 analyzed by log-rank (Mantel-Cox) test. (n=10-14; $**P < 0.01$).
729 (H) Kaplan-Meier survival curve of *Ifnar1*$^{fl/fl}$, *Cd64*^{Cre}*Ifnar1*$^{fl/fl}$, *LysM*^{Cre}*Ifnar1*$^{fl/fl}$, *and*
730 *Cd4*^{Cre}*Ifnar1*$^{fl/fl}$. Survival data were analyzed by log-rank (Mantel-Cox) test. (n=9-14; $*P < 0.05$,
731 $****P < 0.0001$).
732 (I) Tumor volumes of mice separated by group over days post treatment.

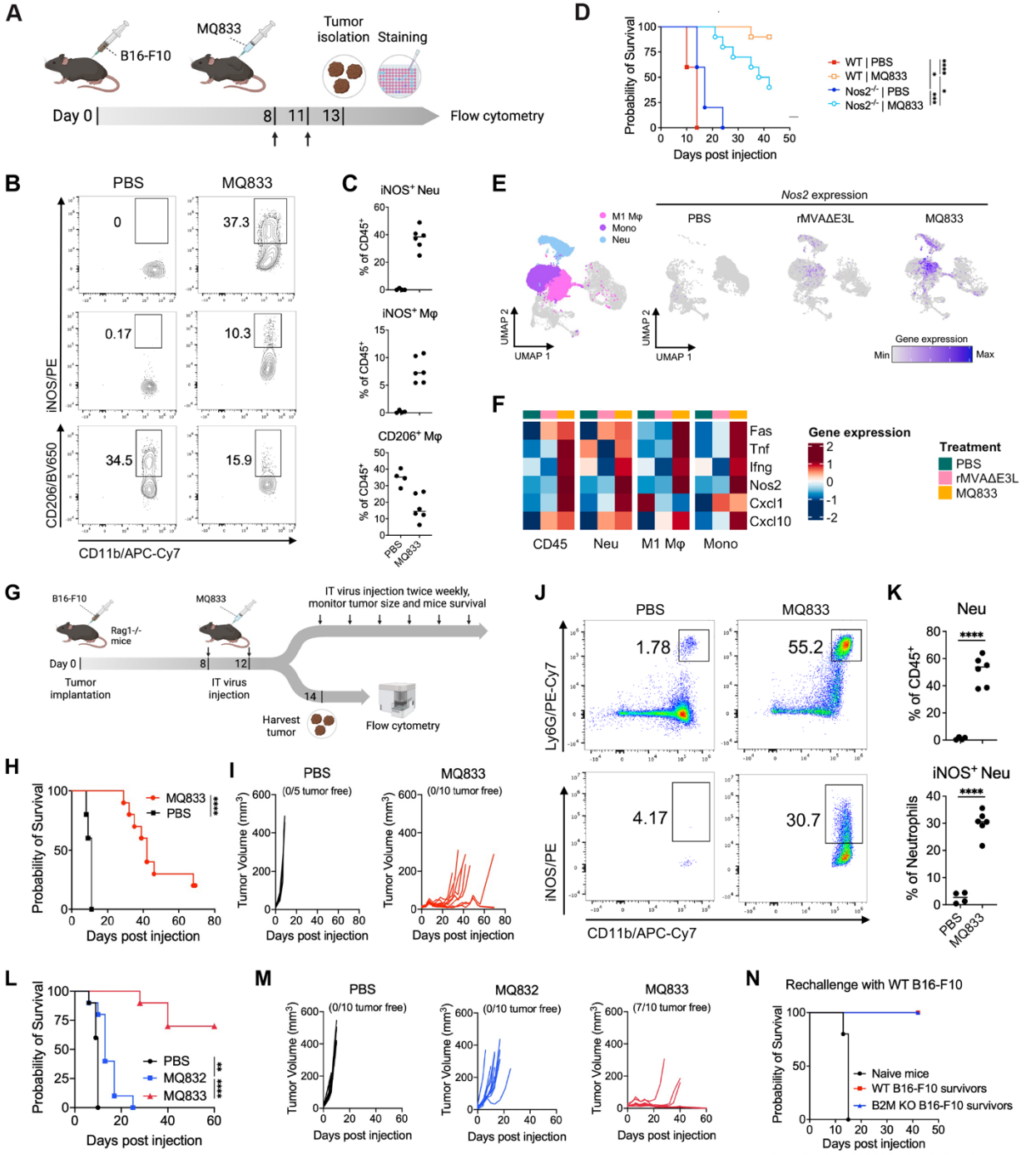
A
B16-F10
MQ833
Tumor isolation
Staining
Day 0
8
11
13
Flow cytometry
B
PBS
MQ833
0
37.3
0.17
10.3
34.5
15.9
iNOS/PE
CD206/BV650
CD11b/APC-Cy7
C
iNOS+ Neu
iNOS+ Mφ
CD206+ Mφ
% of CD45+
PBS
MQ833
D
Probability of Survival
Days post injection
WT | PBS
WT | MQ833
Nos2-/- | PBS
Nos2-/- | MQ833
E
Nos2 expression
M1 Mφ
Mono
Neu
PBS
rMVAΔE3L
MQ833
UMAP 2
UMAP 1
Gene expression
Min
Max
F
Fas
Tnf
Ifng
Nos2
Cxcl1
Cxcl10
CD45
Neu
M1 Mφ
Mono
Gene expression
Treatment
PBS
rMVAΔE3L
MQ833
G
B16-F10
Rag1-/- mice
MQ833
IT virus injection twice weekly, monitor tumor size and mice survival
Day 0
8
12
14
Tumor implantation
IT virus injection
Harvest tumor
Flow cytometry
H
Probability of Survival
MQ833
PBS
Days post injection
I
PBS
(0/5 tumor free)
MQ833
(0/10 tumor free)
Tumor Volume (mm3)
Days post injection
J
PBS
MQ833
1.78
55.2
4.17
30.7
Ly6G/PE-Cy7
iNOS/PE
CD11b/APC-Cy7
K
Neu
% of CD45+
iNOS+ Neu
% of Neutrophils
PBS
MQ833
L
Probability of Survival
PBS
MQ832
MQ833
Days post injection
M
PBS
(0/10 tumor free)
MQ832
(0/10 tumor free)
MQ833
(7/10 tumor free)
Tumor Volume (mm3)
Days post injection
N
Rechallenge with WT B16-F10
Probability of Survival
Naive mice
WT B16-F10 survivors
B2M KO B16-F10 survivors
Days post injection

733 **Figure 7. *Nos2*-dependent myeloid activation contributes to MQ833-induced antitumor**
734 **immunity**
735 (A) Schematic diagram of the flow cytometry analysis experiment.
736 (B and C) Contour plots (B) and dot plots (C) showing percentage of $iNOS^+$ cells among
737 $CD45^+CD3^-CD11b^+Ly6g^+$ neutrophils (top row), $CD45^+CD3^-CD68^+CD11b^+$ macrophages
738 (middle row), and percentage of $CD206^+$ cells among macrophages (bottom row) in MQ833 or
739 PBS treated tumors.
740 (D) Kaplan-Meier survival curve of mice in each treatment group. Survival data were analyzed
741 by log-rank (Mantel-Cox) test. (n=5-10; $*P < 0.05$, $***P < 0.001$, $****P < 0.0001$)
742 (E and F) scRNA-seq analysis of $CD45^+$ cells isolated from rMVAΔE3L or MQ833 treated
743 tumors. (E) UMAP display showing *Nos2* expression (right panel) in highlighted clusters (left
744 panel) (F) Heatmaps showing average expression of selected antitumor marker genes in all the
745 cells (first panel), neutrophil (second panel), M1 macrophage (third panel), and monocyte (fourth
746 panel) clusters divided by treatment groups.
747 (G) Schematic diagram of the survival and flow cytometry experimental design.
748 (H) Kaplan-Meier survival curve of mice in each treatment group. PBS was used as a control.
749 Survival data were analyzed by log-rank (Mantel-Cox) test. (n=5-10; $****P < 0.0001$) .
750 (I) Tumor volumes of mice separated by group over days post treatment.
751 (J and K) Dot plots (D) and bar graphs (E) showing percentage of $CD45^+CD3^-CD11b^+Ly6g^+$
752 neutrophils among total $CD45^+$ cells (top row) and $iNOS^+$ cells among neutrophils (bottom row)
753 in MQ833 or PBS treated tumors.
754 (L and M) $1x10^6$ of $B2m^{-/-}$ B16-F10 cells were intradermally implanted into the right flank of
755 WT C57BL/6J mice. (L) Kaplan-Meier survival curve of mice in each treatment group. PBS was
756 used as a control. (n=10) Survival data were analyzed by log-rank (Mantel-Cox) test. (n=10; $**P$
757 < 0.01, $****P < 0.0001$). (M) Tumor volumes of mice separated by group over days post
758 treatment.
759 (N) Mice rejected primary B16-F10 or $B2m^{-/-}$ B16-F10 tumors were rechallenged with a lethal
760 dose of B16-F10 tumor cells. Kaplan-Meier survival curve of the rechallenged mice.

761 **METHODS**

762

763 **Mice**

764 Female C57BL/6J mice between 6 and 8 weeks of age were purchased from the Jackson
765 Laboratory (Strain #000664) were used for the preparation of bone marrow-derived dendritic
766 cells and for *in vivo* experiments. These mice were maintained in the animal facility at the Sloan
767 Kettering Institute. All procedures were performed in strict accordance with the
768 recommendations in the Guide for the Care and Use of Laboratory Animals of the National
769 Institutes of Health. The protocol was approved by the Committee on the Ethics of Animal
770 Experiments of Sloan Kettering Cancer Institute. *Sting*$^{Gt/Gt}$ mice were generated in the laboratory
771 of Dr. Russell Vance (University of California, Berkeley).[39] *cGas*$^{-/-}$ (Strain #026554),[40] *Stat2*$^{-/-}$
772 (Strain #023309)[41] and *Nos2*$^{-/-}$ (Strain #002609)[42] mice were purchased from Jackson Laboratory.
773 *Mda5*$^{-/-}$ mice were generated in Marco Colonna's laboratory (Washington University).[43] *Mda5*$^{-/-}$
774 *Sting*$^{Gt/Gt}$ were bred in our lab.[44] *CD64*^{cre} (as known as *Fcgr1-cre)* mouse stain was generated in
775 Dr. Ming O. Li's laboratory (Memorial Sloan Kettering Cancer Center). *Ifnar1*$^{fl/fl}$ (Strain #
776 028256), *Mrp8*^{cre} (Strain # 021614)[45,], *LysM*^{cre} (Strain #004781),[46] and *CD4*^{cre} (Strain #017336)[47]
777 mice were also purchased from Jackson Laboratory. *Mrp8*^{cre}*Ifnar1*$^{fl/fl}$, *Cd64*^{Cre}*Ifnar1*$^{fl/fl}$,
778 *LysM*^{Cre}*Ifnar1*$^{fl/fl}$, *and Cd4*^{Cre}*Ifnar1*$^{fl/fl}$ were bred in our lab.

779

780 **Cell lines**

781 BHK-21 (baby hamster kidney cell, ATCC CCL-10) cells were cultured in Eagle's minimal
782 essential medium containing 10% fetal bovine serum (FBS), 0.1 mM nonessential amino acids,
783 penicillin, and streptomycin. The murine melanoma cell line B16-F10 was originally obtained
784 from I. Fidler (MD Anderson Cancer Center). MC38 cell line was obtained from ATCC. The
785 B16-F10 cell line was maintained in RPMI-1640 medium supplemented with 10% FBS, 0.05
786 mM 2-mercaptoethanol, penicillin, and streptomycin. The B16-F10 cell line lacking B2M gene
787 were generated by using CRISPR-cas9 technology. MB49-luc cell line was a kind gift from
788 Michael Glickman (Memorial Sloan Kettering Cancer Center).

789

790 **Viruses**

791 The MVA virus was a kind gift from Gerd Sutter (University of Munich). MVAΔE5R,
792 MVAΔE5R-hFlt3LmOX40L (rMVA), rMVAΔE3L, rMVAΔE3LΔWR199 (MQ832),
793 rMVAΔE3LΔWR199-IL12 (MQ833), and hMQ833 were generated by transfecting pUC57-
794 based plasmids into BHK-21 cells that were infected with MVA at MOI 0.05. Recombinant
795 viruses were purified after 4~6 rounds of plaque selection based on the fluorescence marker.
796 PCR and DNA sequencing were performed to verify the purity of the recombinant viruses.
797 Viruses were propagated in BHK-21 cells and purified through a 36% sucrose cushion.
798
799 **Human monocyte-derived dendritic cell (moDC) generation and T cell isolation**
800 All collection and use of human specimens adhered to protocols reviewed and approved by the
801 Institutional Review and Privacy Board of Memorial Hospital, MSKCC. Buffy coat products
802 were obtained from healthy donor at New York Blood Center and peripheral blood mononuclear
803 cells (PBMCs) separated by standard centrifugation over Ficoll-Paque PLUS (Amersham
804 Pharmacia Biotech, Uppsala, Sweden). Tissue culture plastic adherent PBMCs comprised the
805 moDCs precursors, which were cultured in complete PRMI 1640-1% human serum
806 supplemented with 1000 IU/ml GM-CSF (PeproTech) and 500 IU/ml IL-4 (PeproTech).
807 Fresh medium and cytokines were replenished every 48 h. T cells were obtained from tissue
808 culture nonadherent PBMCs, then further purified by $CD8^+$ T cell or $CD4^+$ T cell isolation kit
809 (Miltenyi Biotec) following manufacturer's instruction.
810
811 **Tumor processing and flow cytometry staining**
812 Tumor samples were collected in cold RPMI and thoroughly chopped into small pieces with
813 surgical scissor. Then we added Liberase TL (1.67 Wünsch U/ml) and DNase I (0.2 mg/ml) to
814 the tube and incubated in 37 °C shaker for 20-30 minutes. Digested tumors were then transferred
815 to GentleMACs C Tube and homogenized using the Gentle MACs Octo Dissociator (Miltenyi
816 Biotec) according to manufacturer's instruction. Samples were then filtered through 70 um filter
817 and quenched with 10 ml cold PBS and spun down. Cells were then washed with MACS buffer
818 (Miltenyi Biotec) twice, and stained with Fc block (BD), viability dye eFluor506 (eBioscience),
819 and cell surface antibodies diluted in MACS buffer for 30 minutes on ice in the dark, and
820 subsequently fixed and permeabilized using the Foxp3 fixation and permeabilization kit (Thermo

821 Fisher). Cells were then incubated with intracellular antibodies diluted in permeabilization buffer
822 for 30 minutes or overnight.
823
824 The following antibodies were used for flow cytometric staining: CD45 Pacific blue (clone 30-
825 F11, Biolegend), CD3 BUV395 (clone 145-2C11, BD), CD4 BUV737 (clone RM4-5, BD), CD8
826 Alexa Fluor 700 (clone 53-6.7, Biolegend), OX40 BV605 (clone OX-86, Biolegend), TIM3
827 BV711 (clone RMT3-23, Biolegend), PD-1 AF647 (clone RMPI-30, BD), KLRG1 APC-Cy7
828 (clone 2F1/KLRG1, Biolegend), Foxp3 PerCP-Cy5.5 (clone FJK-16s, Invitrogen), Ki67 BV786
829 (clone B56, BD), TOX PE (clone REA473, Miltenyi Biotec), Granzyme B PE-Texas red (clone
830 GB11, Invitrogen), CD11b APC-eFluor780 (clone M1/70, eBioscience), Ly6G PE-Cy7 (clone
831 1A8, BD), F4/80 APC (clone BM8, Biolegend), CD68 BV421 (clone FA-11, Biolegend), iNOS
832 PE (clone W16030C, Biolegend).
833
834 After staining, cells were washed and resuspended with MACS buffer and transferred into FACS
835 tubes with 70 um filter caps. Single cell suspensions were run on Cytek Aurora analyzer, and the
836 data was analyzed with Flowjo.
837
838 **Generation of bone marrow-derived dendritic cells**
839 Bone marrow cells were extracted from the femur and tibia of mice. After centrifugation, cells
840 were re-suspended in ACK Lysing Buffer (Lonza) for red blood cell lysis by incubating the cells
841 on ice for 1-3 min. Cells were then resuspended in fresh medium and filtration through a 70-µm
842 cell strainer (BD Biosciences). For the generation of Flt3L-BMDCs, the bone marrow cells (5
843 million cells in each well of 6-well plates) were cultured in complete medium (CM) in the
844 presence of Flt3L (100 ng/ml; R & D systems) for 7–9 days. Cells were fed every 2–3 days by
845 replacing 50% of the old medium with fresh medium. For the generation of GM-CSF-BMDCs,
846 the bone marrow cells (5 million cells in each 15 cm cell culture dish) were cultured in RPMI-
847 1640 medium supplemented with 10% fetal bovine serum (FBS) in the presence of 30 ng/ml
848 GM-CSF (BioLegend) for 9-12 days. Fresh medium and cytokine were replenished every 2-3
849 days.
850
851 **RNA isolation and Real-time PCR**

852 Cells were infected with various viruses at a MOI of 10 for 1 hour or mock-infected. The
853 inoculum was removed, and the cells were washed with PBS twice and incubated with fresh
854 medium for 16 hours or overnight. RNA was extracted from whole-cell lysates with RNeasy Plus
855 Mini kit (Qiagen) and was reverse-transcribed with cDNA synthesis kit (Thermo Fisher). Real-
856 time PCR was performed in triplicate with SYBR Green PCR Master Mix (Life Technologies)
857 and Applied Biosystems 7500 Real-time PCR Instrument (Life Technologies) using gene-
858 specific primers. Relative expression was normalized to the levels of glyceraldehyde-3-
859 phosphate dehydrogenase (GAPDH). The primer sequences for quantitative real-time PCR are
860 listed in Table S1.
861
862 **ELISA**
863 For IL-12 transgene expression verification, B16 cells were infected with MVAΔE5R or MQ833
864 at a MOI of 10 for 1 hour. Mock-infected cells were used as a control. The supernatant was
865 removed, and the cells were washed with PBS twice and incubated with fresh medium for 16
866 hours. Supernatant was collected from the culture, and IL-12 levels were determined using
867 Duoset ELISA kit (R&D) following manufacturer's instruction.
868 For T cell activation assays, supernatant from the co-culture system were collected and IFNγ
869 levels were determined by Duoset ELISA kit (R&D).
870
871 **ELISPOT assay**
872 Spleens were harvested from mice treated with different viruses and were mashed through a
873 70 µm strainer (Thermo Fisher Scientific). Red blood cells were lysed using ACK Lysis Buffer
874 (Life Technology), and the cells were then resuspended in RPMI medium. Enzyme-linked
875 ImmunoSpot (ELISPOT) assay was performed to measure IFN-γ+ CD8+ T cells, according to
876 the manufacturer's protocol (BD Bioscience). 1×10^6 splenocytes were co-cultured with 2.5×10^5
877 irradiated B16-F10 in complete RPMI medium overnight. IFNγ+ splenocytes were detected by
878 Mouse IFNγ ELISPOT kit (BD Biosciences)
879
880 **Western blot analyses**
881 B16-F10 cells or [39]were infected with MQ832 or MQ833 at a MOI of 10 for 1 hour. Mock-
882 infected cells were used as a control. Cells were then washed with PBS twice and cultured with

883 fresh medium. Cells were lysed in RIPA lysis buffer supplemented with 1x Halt™ Protease and
884 Phosphatase Inhibitor Cocktail at indicated time points. Protein samples were separated by SDS-
885 PAGE and then transferred to nitrocellulose membrane. Primary antibodies specific for phospho-
886 IRF3 (1:500, CST, 4947), IRF3 (1:1000, CST, 4302), cGAS (1:1000, CST, 31659), STING
887 (1:1000, CST, 13647), phospho-STING (1:500, CST, 72971), TBK1 (1:1000, CST, 3504), and
888 phosphor-TBK1 (1:500, CST, 5483) were used. GAPDH antibody (1:5000, CST, 2118) were
889 used as loading controls. Anti-rabbit HRP-linked IgG antibody was used as a secondary antibody
890 (1:5000, CST, 7074). Detection was performed using SuperSignalTM Substrates (Thermo
891 Fisher, 34096 or A38555).
892
893 **In vitro T cell activation assay**
894 For murine MQ833, splenic CD11c+ DCs were sorted from WT mice and subsequently infected
895 with various viruses at a MOI of 10 for 1 hour and pulsed with OVA (1.25 mg/ml). OT-1 T cells
896 were isolated from the spleens OT-1 mice using negative selection with $CD8a^+$ T Cell Isolation
897 Kit (Miltenyi Biotec) according to the manufacturer's instructions. OT-1 T cells were then co-
898 cultured with DCs (DC:T = 1:5) for 3 days. Alternatively, T cells were incubated with
899 supernatant collected from the infected $CD11c^+$ DCs for 3 days. IFN-γ levels in the supernatants
900 were determined by ELISA.
901
902 For human MQ833, human moDCs were infected with various viruses at a MOI of 10 for 1 hour
903 and pulsed with OVA (1.25 mg/ml). CD8 or CD4 T cells were purified from human PBMCs
904 using isolation kits (Miltenyi Biotec) following manufacturer's instruction. T cells and moDCs
905 were co-cultured (DC:T = 1:15) for 3 days and supernatant were then collected for IFN-γ ELISA.
906
907 **Tumor challenge and treatment**
908 For survival experiments, 5×10^5 B16-F10 cells, 5×10^5 MC38 cells, 1×10^6 $B2m^{-/-}$ B16 cells were
909 implanted intradermally into the shaved skin on the right flanks of mice. 1×10^6 MB49-luc cells
910 were implanted subcutaneously into the right flanks of mice. Once the tumors are 3 mm in
911 diameter or larger, they were injected with 4×10^7 PFU of MQ832, MQ833 or PBS when the mice
912 were under anesthesia. Viruses were injected twice weekly as specified in each experiment and
913 tumor sizes were measured twice a week. For combination therapy with ICBs, the following

914 antibodies were injected interperitoneally twice weekly: anti-CTLA-4 (100 µg per mouse), Anti-
915 PD-L1 (200 µg per mouse), anti-PD-1 (200 per mouse), or isotype control antibody. Tumor
916 volumes were calculated according to the following formula: l (length) × w (width) × h
917 (height)/2. Mice were euthanized for signs of distress or when the diameter of the tumor reached
918 10 mm.
919
920 In the bilateral tumor implantation model, B16-F10 or MC38 cells were implanted intradermally
921 into right (5×10^5) and left (1×10^5) flanks of C57BL/6J mice. After 7 days after implantation
922 when the tumors were established, the tumors at the right flank were injected with 4×10^7 PFU of
923 MQ832, MQ833 or PBS twice weekly.
924
925 For the tumor rechallenge study, the survived mice (more than 60 days after initiation of
926 intratumoral virotherapy) were rechallenged with intradermal delivery of a lethal dose of B16-
927 F10, MB49 or B2m KO B16-F10 (5×10^5 cells) at the contralateral side.
928
929 For flow cytometric analysis and single cell RNA-seq, 5×10^5 B16-F10 tumor cells were
930 implanted intradermally into the right flanks of the mice for the unilateral tumor implantation
931 model. For bilateral implantation, 5×10^5 and 2.5×10^5 B16-F10 tumor cells were implanted
932 intradermally into the right and left flanks of mice. At 8-11 days after implantation when tumors
933 were established, the tumors at the right flank were injected with 4×10^7 PFU of MQ832,
934 MQ833, or PBS once, or twice with 3 days apart. Tumors were harvested two days after second
935 injection.
936
937 **Purification of anti-CSF-1 monoclonal antibody**
938 The anti-CSF-1 monoclonal antibody (clone 5A1) was purified from cell supernatant of
939 hybridoma (ATCC, #CRL-2702) 1,2. Briefly, hybridoma cells were cultured in Hybridoma-SFM
940 medium (Thermo #12045076) for 3 weeks to produce antibody. Cell supernatant was collected to
941 do antibody purification by using LigaTrap Rat IgG purification column (LigaTrap Technologies
942 #LT-138) according to the manufacturer's procedure. Antibody quality and concentration were
943 examined by SDS-PAGE gel electrophoresis and nanodrop, respectively.
944

945 **In vivo antibody depletion experiment**

946 Immune cell subsets were depleted by administering 200 μg monoclonal antibodies i.p. twice
947 weekly starting 1 day prior to the first viral injection as indicated, continued until the animals
948 either died, were euthanized, or were completely clear of tumors: anti-CD8-α for CD8+ T cells
949 (clone 2.43, BioXCell), anti-CD4 for $CD4^+$ T cells (clone GK1.5, BioXCell), anti-NK1.1 for NK
950 cells (clone PK136, BioXCell). 500 μg of anti-Ly6G (clone 1A8, BioXCell) were given for
951 neutrophil depletion. 500 μg of anti-CSF1 (provided by Ming Li's laboratory) were given every
952 5 days for macrophage depletion. Depletion efficacies of CD8 T cells, CD4 T cells, NK cells and
953 neutrophils were confirmed by flow cytometry of peripheral blood.

954

955 **Cell sorting for tumor infiltrating immune cells**

956 Tumors were harvested and single cell suspensions were prepared. Cells were then stained with
957 Cell Viability Dye (eFlour506, brand) and anti-CD45 antibody (brand). $CD45^+$ live cells were
958 then sorted using B&D Aria cell sorter.

959

960 **Single-cell RNA-sequencing and data analysis.**

961 *Library preparation and sequencing*

962 $CD45^+$ populations from tumors were purified by FACS sorting. We performed single-cell 5′
963 gene expression profiling on the single-cell suspension using the Chromium Single Cell V(D)J
964 Solution from 10x Genomics according to the manufacturer's instructions. Cell-barcoded 5′ gene
965 expression libraries were sequenced on an Illumina NovaSeq6000 sequencer with pair-end reads.

966

967 *Gene expression UMI counts matrix generation*

968 The sequencing data were primarily analyzed by the 10× cellranger pipeline (v3.0.2) in two
969 steps. In the first step, cellranger mkfastq demultiplexed samples and generated fastq files; and in
970 the second step, cellranger count aligned fastq files to the reference genome and extracted gene
971 expression UMI counts matrix. In order to measure both human and viral gene expression, we
972 built a custom reference genome by integrating the MVA virus genome into the 10× pre-built
973 mouse reference using cellranger mkref. The MVA virus genome was downloaded from NCBI.

974

975 *Single-cell RNA-seq data analysis*

976 All cells expressing <200 or >6,000 genes were removed as well as cells that contained >5%
977 mitochondrial counts. Samples were merged and normalized. The default parameters of Seurat
978 were used, unless mentioned otherwise. Briefly, 2,000 variable genes were identified for the
979 clustering of all cell types and principal component analysis (PCA) was applied to the dataset to
980 reduce dimensionality after regressing for the number of UMIs (counts). The top 12-15 most
981 informative principal components (PCs) were used for clustering and Uniform Manifold
982 Approximation and Projection for dimension reduction (UMAP). To characterize each cluster,
983 we applied both the *FindAllMarkers* and *FindMarkers* procedure in Seurat, which identified
984 markers using log fold changes (FC) of mean expression. To identify differentially expressed
985 genes between two groups of clusters, *FindMarkers* functions in Seurat and Enhanced Volcano R
986 package (v1.8.0) were used. For subsequent T cell analysis, we first extracted all the $CD3^+$ cells
987 from the original dataset and repeated the clustering procedures in the T cell subset.
988
989 *Gene set enrichment analysis (GSEA)*
990 The GSEA analysis was done and visualized using the *clusterProfiler* (v4.0.5) and *enrichplot*
991 (v1.12.3) packages, which uses predefined gene sets from the Molecular Signatures Database
992 (MSigDB v7.4) [48]. We used the hallmark gene sets collection for the present study. Genes were
993 ranked by the test statistic value obtained from differential expression analysis and the pre-
994 ranked version of the tool was used to identify significantly enriched biological pathways.
995
996 Statistical analysis
997 Two-tailed unpaired Student's t test was used for comparisons of two groups in the studies.
998 Survival data were analyzed by log-rank (Mantel-Cox) test. The p values deemed significant are
999 indicated in the figures as follows: *, $p < 0.05$; **, $p < 0.01$; ***, $p < 0.001$; ****, $p < 0.0001$.
1000 The numbers of animals included in the study are discussed in each figure legend.
1001
1002 **Lead Contact**
1003
1004 Further information and requests for resources and reagents used in this study should be directed
1005 to and will be fulfilled by the lead contact and the corresponding author, Liang Deng
1006 (dengl@mskcc.org).

1007 **Materials availability**
1008
1009 Materials generated in our laboratory are available upon request.
1010

1011 **Data and code availability**

1012 The RNA-seq data reported in this study will be deposited in GEO and made publicly available
1013 prior to journal publication.
1014

1015 **Acknowledgements**

1016 We thank the Flow Cytometry Core Facility and Molecular Cytology Core Facility at the Sloan
1017 Kettering Institute and Genomic core at Weill Cornell Medical College. This work was
1018 supported by MSK Technology Development Fund (L.D.), Sponsored Research Agreement from
1019 IMVAQ Therapeutics (L.D.), Cycle for Survival (L.D.), Center for Experimental Therapeutics at
1020 Memorial Sloan Kettering Cancer Center (L.D.), Melanoma Research Alliance (L.D.), and SNF
1021 Institute for Global Infectious Disease Research (C.M.R.). This work was supported in part by
1022 the Swim across America (J.D.W., T.M.), Ludwig Institute for Cancer Research (J.D.W., T.M.),
1023 Parker Institute for Cancer Immunotherapy, Weill Cornell Medicine (J.D.W., T.M.). This
1024 research was also funded in part through the NIH/NCI Cancer Center Support Grant P30
1025 CA008748.
1026

1027 **Author Contributions**

1028 S.T.L., Y.Q.W., and G.M. contributed to project conception, experimental design, execution of
1029 experiments, data analysis, interpretation, and manuscript writing. S.B.T., J.A.L., Y.W., and
1030 N.Y. assisted with mouse experiments and data analysis. S.T.L., Y.Q.W., T.Z., and A.T.
1031 analyzed the single-cell RNA-seq data. L.L.J. and M.O.L. provided the anti-CSF1 antibody and
1032 the CD64cre mouse strain. C.M.R., J.D.W., T.M., D.H., M.O.L., W.Y., J.C., J.H.W., and J.Z.X.
1033 provided input on experimental design, data interpretation, and manuscript editing. All authors
1034 contributed to manuscript preparation. L.D. supervised all aspects of the study.
1035

1036 **Competing interests**

1037 Memorial Sloan Kettering Cancer Center (MSKCC) filed a patent application for the use of
1038 recombinant MVA as monotherapy or in combination with immune checkpoint blockade for the

1039 treatment of solid tumors. MSKCC has granted Fix Therapeutics an exclusive option to this
1040 intellectual property. J.D.W. is a consultant of Ankyra Therapeutics, Apricity; Arsenal
1041 Biosciences, Ascentage Pharma, Bristol Myers Squibb, Daiichi Sankyo, Immunogenesis,
1042 Takeda, Tizona, Immunocore – Data Safety board, and Scancell. J.D.W. received
1043 Grant/Research Support from: Bristol Myers Squibb. J.D.W. has Equity in: Apricity, CellCarta,
1044 Ascentage, Imvaq, Linneaus, Georgiamune, Tizona Therapeutics, and Xenimmune. T.M. acted
1045 in the capacity of consultant for Immunos Therapeutics, Daiichi Sankyo Co, TigaTx, Normunity
1046 and Pfizer. T.M. has received research support from Surface Oncology, Kyn Therapeutics,
1047 Infinity Pharmaceuticals, Peregrine Pharmaceuticals, Adaptive, Biotechnologies, Leap
1048 Therapeutics, Aprea Therapeutics, Enterome SA and Realta Life Sciences, and currently receives
1049 research funding from Bristol Myers Squibb. L.D., J.D.W., T.M., W.Y., J.C., and N.Y.
1050 are cofounders of and equity holders in IMVAQ Therapeutics.